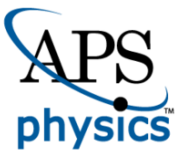

Synchronization of spatially discordant voltage and calcium alternans in cardiac tissue

Chunli Huang, Zhen Song, and Zhilin Qu

Phys. Rev. E **106**, 024406 — Published 11 August 2022

DOI: 10.1103/PhysRevE.106.024406

Synchronization of spatially discordant voltage and calcium alternans in cardiac tissue

Chunli Huang[1,2], Zhen Song[3], Zhilin Qu[2,4,*]
[1]*School of Mathematics and Statistics, Guangdong University of Foreign Studies, Guangzhou 510420, China*
[2]*Department of Medicine, University of California, Los Angeles, California 90095, USA*
[3]*Peng Cheng Laboratory, Shenzhen, Guangdong, China*
[4]*Department of Computational Medicine, University of California, Los Angeles, California 90095, USA*
(Received date)

The heart is an excitable medium which is excited by membrane potential depolarization and propagation. Membrane potential depolarization brings in calcium (Ca) through the Ca channels to trigger intracellular Ca release for contraction of the heart. Ca also affects voltage via Ca-dependent ionic currents, and thus voltage and Ca are bidirectionally coupled. It has been shown that the voltage subsystem or the Ca subsystem can generate their own dynamical instabilities which are affected by their bidirectional couplings, leading to complex dynamics of action potential and Ca cycling. Moreover, the dynamics become spatiotemporal in tissue in which cells are diffusively coupled through voltage. A widely investigated spatiotemporal dynamics is spatially discordant alternans (SDA) in which action potential duration (APD) or Ca amplitude exhibits temporally period-2 and spatially out-of-phase patterns, i.e., APD-SDA and Ca-SDA patterns, respectively. However, the mechanisms of formation, stability, and synchronization of APD-SDA and Ca-SDA patterns remain incompletely understood. In this study, we use cardiac tissue models described by amplitude equation, coupled iterated maps, and reaction-diffusion equations with detailed physiology (the ionic model) to perform analytical and computational investigations. We show that when the Ca subsystem is stable, the Ca-SDA pattern always follows the APD-SDA pattern and thus they are always synchronized. When the Ca subsystem is unstable, synchronization of APD-SDA and Ca-SDA patterns depends on the stabilities of both subsystems, their coupling strengths, and the spatial scales of the initial Ca-SDA patterns. Spontaneous (initial condition-independent) synchronization is promoted by enhancing APD instability and reducing Ca instability as well as stronger Ca-to-APD and APD-to-Ca coupling, a pattern formation caused by dynamical instabilities. When Ca is more unstable and APD is less unstable or APD-to-Ca coupling is weak, synchronization of APD-SDA and Ca-SDA patterns is promoted by larger initially synchronized Ca-SDA clusters, i.e., initial condition-dependent synchronization. The synchronized APD-SDA and Ca-SDA patterns can be locked in-phase, anti-phase, or quasiperiodic depending on the coupling relationship between APD and Ca. These theoretical and simulation results provide mechanistic insights into the APD-SDA and Ca-SDA dynamics observed in experimental studies.
DOI:

I. Introduction

The function of the heart is to pump blood via mechanical contraction and relaxation. Contraction and relaxation of the heart are regulated by intracellular calcium (Ca) which rises and decays following the membrane potential depolarization and repolarization cycle. This process is called excitation-contraction coupling [1]. On the other hand, the membrane potential or voltage is also affected by Ca via Ca-dependent ionic currents, and thus Ca and voltage are bi-directionally coupled. Complex action potential duration (APD) and Ca cycling dynamics can occur due to instabilities originating from the voltage subsystem (voltage-driven) or the Ca subsystem (Ca-driven), as well as their bidirectional couplings [2]. Alternans, a period-2 behavior, is the most widely investigated nonlinear dynamics in cardiac systems, including animal experiments and clinical settings [3-12]. Theoretical and simulation studies have shown that alternans can arise from instabilities originating from voltage [6, 7, 13] or Ca cycling [14-20], which can be potentiated or attenuated by the bidirectional couplings of the two [21-23]. Both voltage-driven alternans and Ca-driven alternans have been demonstrated in experimental studies [6, 24-30]. Since voltage and Ca are coupled, voltage-driven alternans can result in Ca alternans and Ca-driven alternans can result in APD alternans. Clinically, alternans manifests in the hearts as either pulsus (mechanical) alternans or T-wave (electrical) alternans. Pulsus alternans and T-wave alternans are widely known as precursors of lethal ventricular arrhythmias and sudden cardiac death [3, 4, 9, 10, 12]. A potential mechanism linking alternans to arrhythmias is spatially discordant alternans (SDA) [31-37] in which APD or Ca exhibits a temporally period-2 but spatially out-of-phase (or anti-phase) behavior (see Fig.1), referring to as APD-SDA and Ca-SDA in this study, respectively. APD-SDA results in large APD gradients, making the tissue susceptible to conduction block and formation of spiral waves [31, 33] or generation of arrhythmia triggers [38]. Therefore, understanding the mechanisms of SDA can provide insights into the understanding of cardiac arrhythmogenesis.

The genesis of APD-SDA has been widely investigated in previous studies [33, 39-41], which mainly focus on the role of conduction velocity (CV) restitution (CVR). CVR is an action potential conduction property in which CV changes as the diastolic interval (DI) changes due to incomplete recovery of the sodium current or changes in excitability [32, 33, 42, 43]. The role of CVR in APD-SDA is supported by some of the experiments [24, 44-47] but not by others [47-49]. In recent simulation and theoretical studies [50, 51], we performed systematic analyses on the roles of CVR, tissue heterogeneities, convection due to conduction, and nodal line curvature in the genesis and

dynamics of APD-SDA, which provide additional theoretical insights for those experiments that do not support the mechanism of CVR-indued APD-SDA. However, these theoretical studies do not take into account the condition when Ca-driven alternans is also present. Since Ca and voltage are bidirectionally coupled, when APD alternans becomes spatially discordant, Ca alternans may also be spatially discordant, or vice versa. Experimental studies [44, 48, 49, 52] have shown that during SDA, the nodal lines of APD-SDA may or may not co-localize with those of the Ca-SDA, i.e., the APD-SDA and Ca-SDA may or may not synchronize with each other. Fig.1 shows such an example from optical mapping experiments in a rabbit heart by Hayashi et al [44]. In this example, the APD-SDA nodal lines co-localize with the Ca-SDA nodal lines in the upper region of the mapping area but not in the lower region. In the lower region, there are Ca-SDA nodal rings without corresponding APD-SDA nodal rings. This indicates that in the upper region, the Ca-SDA pattern is synchronized with the APD-SDA pattern but not in the lower region. Therefore, there is a key question to be addressed: when and how are APD-SDA patterns and Ca-SDA patterns synchronized in cardiac tissue?

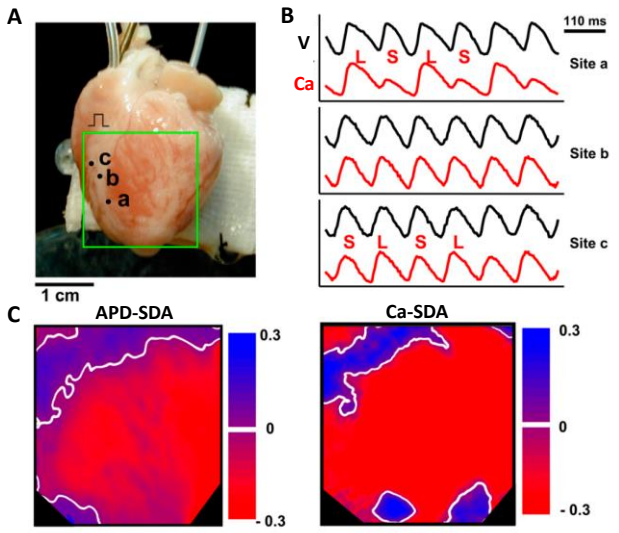

FIG.1. Spatially discordant APD and Ca alternans in a rabbit heart. A. An image of a rabbit heart and the optical mapping area. B. Simultaneous recordings of voltage and Ca from three different sites marked in A. C. Nodal lines (white) in APD alternans map. D. Nodal lines (white) in the Ca alternans map. Modified from Hayashi et al.

Answering this question is important for understanding cardiac arrhythmogenesis [53]. Since a critical APD gradient is needed for reentry initiation [54-57], synchronization of Ca-SDA and APD-SDA patterns is needed for the Ca-driven alternans to result in a large enough APD gradient. In other words, since Ca is not directly coupled between cells (Fig.2A), it can alternate out-of-phase in space. If Ca is not synchronized in space with APD, its effect on APD will be averaged out in space since voltage is diffusively coupled between cells. Previous simulation studies have investigated the formation of SDA in the presence of Ca-driven alternans [44, 58-60], but have not addressed the question of when and how APD-SDA and Ca-SDA patterns can be synchronized. In this study, we perform a systematic theoretical study combined with computer simulations to understand the formation and stability of SDA patterns in the presence of both voltage-driven instability (or voltage-driven alternans) and Ca-driven instability (or Ca-driven alternans), in particular synchronization of the APD-SDA pattern with the Ca-SDA pattern. We use three types of mathematical models of different complexity and physiological details, i.e., the amplitude equation (AE) model with generic kinetics, the coupled map lattice (CML) model incorporating certain physiological properties, and the ionic model (i.e., the rabbit ventricular myocyte model by Mahajan et al [61]) describing the detailed physiological processes. Spatiotemporal APD and Ca dynamics in both one-dimensional (1D) cable and two-dimensional (2D) tissue models are investigated. Through theoretical analyses and computer simulations of these models, we reveal the conditions and mechanisms for the formation and synchronization of APD-SDA and Ca-SDA patterns, which provides mechanistic insights into the formation and synchronization of the APD-SDA and Ca-SDA patterns observed in experimental studies.

II. Methods and materials

A. Mathematical models

The AE model is described in the corresponding section in Results. Details of the CML model and the ionic model are described in Appendix.

B. Voltage and Ca coupling

Fig.2A is a schematic plot for voltage and Ca coupling and cell-to-cell coupling in cardiac tissue. In cardiac tissue, the cells are electrically coupled via ion channels called gap junctions. When one cell depolarizes, the voltage differences between this cell and its neighbors result in current flows to its neighbors, causing the neighboring cells to depolarize. Although Ca may also pass through the gap junction to cause cell-to-cell Ca coupling [62], it is believed that this coupling is very weak, which is omitted in computational cardiac tissue models. Here we also assume that there is no cell-to-cell Ca coupling, and the cells are coupled only via voltage.

Ca and voltage are bidirectionally coupled within a cell via the Ca-dependent ionic currents as well as Ca-dependent signaling. We refer the couplings to as Ca-to-APD coupling and APD-to-Ca coupling as detailed below:

1) Ca-to-APD coupling. Ca affects APD via Ca-dependent ionic currents or Ca-dependent signaling which then regulates ionic currents. For example, increasing Ca increases Na-Ca exchange current (I_{NCX}), which is an inward current, prolonging APD. Increasing Ca enhances Ca-dependent inactivation of the L-type Ca current ($I_{Ca,L}$), shortening APD. Increasing Ca also increases the slow component of the delayed rectifier potassium current (I_{Ks}) and the Ca-activated small conductance potassium current

(I_{SK}) [63, 64], which are outward currents activated by Ca, shortening APD. Therefore, increasing Ca can either lengthen or shorten APD (Fig.2B), which results in positive Ca-to-APD coupling or negative Ca-to-APD coupling, respectively.

2) APD-to-Ca coupling. APD affects Ca mainly in two ways. First, lengthening APD affects Ca entry and extrusion via changing $I_{Ca,L}$ and I_{NCX}, which change the Ca load for the next beat. The amount of Ca released is larger for a higher SR Ca load, and this property is called refractional release relationship [65, 66]. Second, lengthening APD shortens DI

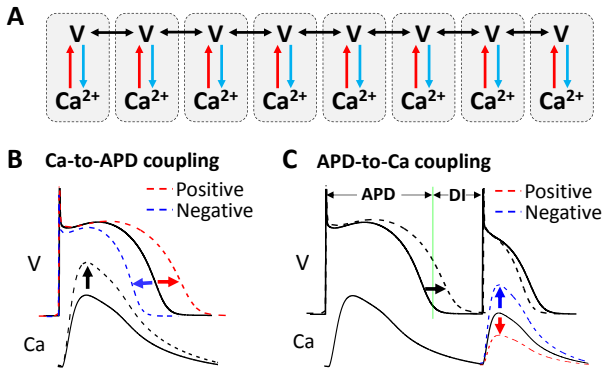

FIG.2. Schematic diagrams of cell-to-cell coupling and Ca and voltage coupling. A. A schematic diagram of coupling between cells and coupling between voltage and Ca in chain of cardiac cells. B. Ca-to-APD coupling. Increasing Ca (black dashed) can either lengthen APD (positive Ca-to-APD coupling) or shorten APD (negative Ca-to-APD coupling). C. APD-to-Ca coupling. Lengthening APD in the 1st beat causes shortening of DI, which may result in either a smaller Ca (positive APD-to-Ca coupling) or a larger Ca (negative APD-to-Ca coupling) in the 2nd beat. See main text for more detailed description.

preceding the next beat, reducing the availability of LCCs as well as that of the Ca release channels, called ryanodine receptors, for opening due to incomplete recovery. Furthermore, the SR Ca load may also be affected by DI due to refilling from the previous release. These effects together give rise to a property called Ca release restitution [67-69]. Therefore, lengthening APD in the present beat can either enhance Ca release or reduce Ca release in the following beat (Fig.2C), resulting in positive APD-to-Ca coupling or negative APD-to-Ca coupling, respectively.

C. Spatially and electromechanically concordant and discordant alternans

When APD (or Ca) alternates in phase in the whole tissue, it is called spatially concordant alternans (SCA). When APD (or Ca) alternates out of phase in space, it is called SDA (Fig.3). During alternans, APD and Ca may alternate either in phase or in anti-phase. In the in-phase mode, a large Ca corresponds to a long APD, and vice versa, which is called electromechanically concordant alternans. In the anti-phase mode, a large Ca corresponds to a short APD, and vice versa, which is called electromechanically discordant alternans. The electromechanically concordant alternans occurs when the Ca-to-APD coupling is positive and electromechanically discordant alternans occurs when the Ca-to-APD coupling is negative.

In the AE model, the variables are the amplitudes of APD and Ca alternans. Furthermore, in the CML model and the ionic model, we present most of the results using the alternans amplitudes. The APD alternans amplitude (Δa_n) is defined as

$$\Delta a_n = (-1)^n (a_{n+1} - a_n)/2 \qquad (1)$$

in which a_n is the APD of the nth beat. The pre-factor $(-1)^n$ maintains the sign of Δa_n during alternans. In other words, the term $(a_{n+1} - a_n)$ changes sign in a beat-to-beat manner during alternans, and the pre-factor keeps Δa_n either positive or negative, unchanged from beat to beat. In a SCA, Δa_n keeps either positive or negative in the whole spatial domain. In a steady-state SDA, the sign of Δa_n remains unchanged in time but changes in space. $\Delta a_n = 0$ corresponds to the SDA node. Similarly, one defines the Ca alternans amplitude (Δc_n) as

$$\Delta c_n = (-1)^n (c_{n+1} - c_n)/2 \qquad (2)$$

c_n is the peak value of the Ca concentration of the nth beat. In the real cardiac myocytes, the intracellular Ca

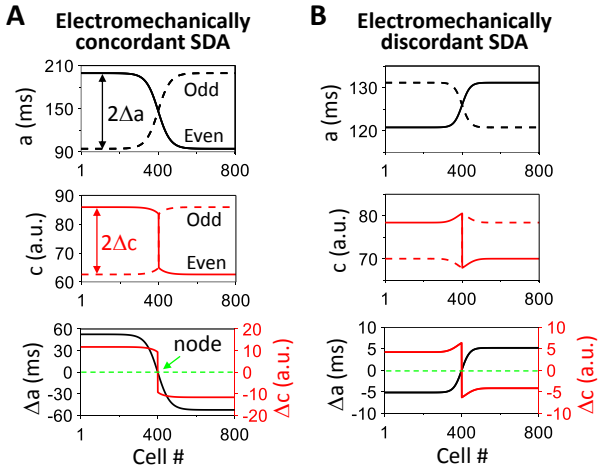

FIG.3. Electromechanically concordant and discordant SDA. A. An example of an electromechanically concordant SDA in which APD and Ca alternate in-phase. Top: APD vs cell # for two consecutive beats. Middle: Peak Ca vs cell # for the same two consecutive beats. Bottom: Alternans amplitude of APD (Δa) and Ca (Δc) calculated from the two beats. B. Same as A but for an electromechanically discordant SDA in which APD and Ca alternate in anti-phase. A and B are simulation results of the CML model (see Appendix) with the following parameters: $T = 250$ ms, $\gamma = 0.002$, $\sigma_R = 0.8$, $\tau_a = 40$, and $\beta = 4$ for A and $T = 250$ ms, $\gamma = -0.002$, $\sigma_R = 0.8$, $\tau_a = 38$, and $\beta = 4.6$ for B.

concentration is in the order of 1 μM. For simplicity, we use an arbitrary unit for c_n and Δc_n but use the real unit millisecond for a_n and Δa_n in the AE model and the CML model. The bottom panels of Fig.3 plot the steady-state patterns of Δa_n and Δc_n from the SDA shown in the top and middle panels. The SDA in Fig.3A is electromechanically concordant in which the signs of Δa_n and Δc_n are the same, i.e., a positive Δa_n corresponds to a positive Δc_n, and a

negative Δa_n corresponds to a negative Δc_n. Fig.3B shows an SDA of electromechanically discordant alternans in which the signs of Δa_n and Δc_n are opposite, i.e., a positive Δa_n corresponds to a negative Δc_n, and vice versa.

D. Pacing protocol

In this study, we pace all cells in the tissue simultaneously, i.e., a global pacing protocol, and thus there is no action potential conduction. As we clarified previously [50, 51], this protocol is not only physiologically realistic, but also a simplified setting that can be helpful for understanding the SDA dynamics in the presence of conduction. We will investigate in a future study the effects of conduction on the SDA dynamics in the presence of Ca alternans using local pacing protocols.

E. Computer simulation methods

Computer simulations are carried out for all three types of models. Numerical simulations of 1D cable and 2D tissue are carried out using a forward Euler method with $\Delta x = 0.0125$ cm, and $\Delta y = 0.0125$ cm. $\Delta t = 0.02$ ms for the AE model and $\Delta t = 0.01$ ms for the ionic model are used. Simulations are carried out by GPU (NVIDIA GeForce RTX 3090) accelerated computing with CUDA C++.

III. Results

A. SDA formation and synchronization in the AE model—Theoretical analyses

The advantage of the AE model is that it is relatively simple so that we can perform analytical treatments, such as stability analysis and theoretical solutions [40, 51, 70]. The first AE model describing voltage-driven SDA dynamics in a 1D cable was derived by Echebarria and Karma [40, 70]. A similar AE model was developed to describe the effects of voltage and Ca coupling on subcellular Ca alternans in single myocytes by Shiferaw and Karma [71]. In a recent study [51], we used the AE model to investigate the voltage-driven SDA dynamics in tissue models under different conditions, such as repolarization and coupling heterogeneities. Here we extend the AE model to describe the SDA dynamics in the presence of Ca-driven alternans by phenomenologically adding an AE describing the amplitude of Ca alternans and the bidirectional coupling effects. Using this AE model, we can perform stability analyses for both SCA and SDA in cardiac tissue and investigate the conditions for synchronization of the APD-SDA and Ca-SDA patterns. The theoretical predictions are then examined using both the CML model and the ionic model that have more physiological parameters and details.

1. The AE model

Under global pacing, the AE model is described by the following coupled partial differential equations:

$$T\frac{\partial \Delta a}{\partial t} = \alpha \Delta a - \beta \Delta a^3 + \gamma \Delta c + \xi^2 \frac{\partial^2 \Delta a}{\partial x^2} \quad (3)$$

$$T\frac{\partial \Delta c}{\partial t} = \rho \Delta c - \varepsilon \Delta c^3 + \sigma \Delta a \quad (4)$$

where T is the pacing period and $t \equiv nT$ with n being the beat number of pacing. In the AE model, the alternans amplitude of APD is treated as a time and space continuous variable, i.e., $\Delta a(x,t)$. α and β, which are related to the slope of the APD restitution curve [40, 70], are the parameters determining the stability and amplitude of the APD alternans in the absence of Ca-driven alternans. In other words, in the absence of Ca-driven alternans (or when Ca and APD are decoupled), when $\alpha < 0$, no APD alternans occurs. When $\alpha > 0$, APD alternans occurs with the steady-state alternans amplitude $\Delta a = \pm\sqrt{\frac{\alpha}{\beta}}$. Similarly, ρ and ε are parameters determining the stability and amplitude of the Ca alternans. Without coupling, when $\rho < 0$, no Ca alternans occurs. When $\rho > 0$, Ca alternans occurs with the steady-state alternans amplitude $\Delta c = \pm\sqrt{\frac{\rho}{\varepsilon}}$. In this study, we fix $\beta = \varepsilon = 0.0001$ but vary α and ρ for stability and alternans.

γ in Eq.3 describes the Ca alternans to APD alternans coupling and σ in Eq.4 describes the APD alternans to Ca alternans coupling, with both couplings assumed to be linear. Note that couplings in Eqs. 3 and 4 are those for Ca and APD alternans amplitudes (i.e., Δa and Δc), not the Ca-to-APD coupling and the APD-to-Ca coupling. However, as illustrated in Fig.2B, for a positive Ca-to-APD coupling, an increase in Ca amplitude lengthens APD, which shortens the APD in the following beat due to a shorter DI, increasing the APD alternans amplitude (Δa). The increase in Ca amplitude also increases the Ca alternans amplitude (Δc). Therefore, a positive Ca-to-APD is equivalent to a positive γ in Eq.3. Similarly, a negative Ca-to-APD coupling corresponds to a negative γ. For the same argument, a positive APD-to-Ca coupling corresponds to a positive σ in Eq.4 and a negative APD-to-Ca coupling corresponds to a negative σ.

To understand the roles of Ca and APD coupling in the genesis of the spatiotemporal dynamics, we first perform a linear stability analysis with the following linearized equations:

$$T\frac{\partial \Delta a}{\partial t} = \alpha \Delta a + \gamma \Delta c + \xi^2 \frac{\partial^2 \Delta a}{\partial x^2} \quad (5)$$

$$T\frac{\partial \Delta c}{\partial t} = \rho \Delta c + \sigma \Delta a \quad (6)$$

Inserting $\begin{pmatrix} \Delta a(x,t) \\ \Delta c(x,t) \end{pmatrix} = \begin{pmatrix} \Delta a_0 \\ \Delta c_0 \end{pmatrix} e^{ikx+\lambda t}$ into Eqs. 5 and 6, one obtains the following Jacobian:

$$J = \begin{pmatrix} \alpha - \xi^2 k^2 & \gamma \\ \sigma & \rho \end{pmatrix} / T \quad (7)$$

whose eigenvalues are:

$$\lambda_k = \frac{(\alpha - \xi^2 k^2 + \rho) \pm \sqrt{(\alpha - \xi^2 k^2 - \rho)^2 + 4\gamma\sigma}}{2T} \quad (8)$$

As indicated in Eq.8, λ_k depends on $\gamma\sigma$. Here we discuss the three coupling cases ($\gamma\sigma = 0$, $\gamma\sigma > 0$, and $\gamma\sigma < 0$) in the sections below.

2. Synchronization of APD-SDA and Ca-SDA patterns when $\gamma\sigma = 0$

We first deal with a special condition, i.e., $\gamma\sigma = 0$. This condition is satisfied when Ca and APD are either completely decoupled ($\gamma = 0$ and $\sigma = 0$) or one-way coupled ($\gamma = 0$ and $\sigma \neq 0$ or $\gamma \neq 0$ and $\sigma = 0$). However, as long as $\gamma\sigma = 0$, the eigenvalues in Eq.8 are decoupled into a voltage-dependent one and a Ca-dependent one, i.e.,

$$\lambda_{k,1} = (\alpha - \xi^2 k^2)/T \text{ and } \lambda_{k,2} = \rho/T \quad (9)$$

Note that $\lambda_{k,2}$ is independent of k, which is due to that Ca is not coupled between cells (Fig.2A). Since the case of $\gamma = 0$ and $\sigma = 0$ (APD and Ca are completely decoupled) is trivial, we discuss the other two cases in detail below.

(a) $\gamma = 0$ *and* $\sigma \neq 0$. In this case, the APD is not affected by Ca but Ca is affected by APD. This condition can be satisfied when the Ca-dependent inward and outward currents are properly balanced so that changing Ca does not change APD, i.e., $\gamma = 0$. Although this condition may be difficult to be satisfied in the real system, it still gives us insights for the condition when the Ca-to-APD coupling is weak, i.e., when γ is small. When $\gamma = 0$, Eqs.3 and 4 become:

$$T\frac{\partial \Delta a}{\partial t} = \alpha\Delta a - \beta\Delta a^3 + \xi^2\frac{\partial^2 \Delta a}{\partial x^2} \quad (10)$$

$$T\frac{d\Delta c}{dt} = \rho\Delta c - \varepsilon\Delta c^3 + \sigma\Delta a(x,t) \quad (11)$$

One can categorize the system into four conditions:

1) When both the APD and the Ca subsystems are stable ($\alpha < 0$ and $\rho < 0$), there is no alternans and thus no SDA patterns.

2) When the APD subsystem is stable and the Ca subsystem is unstable ($\alpha < 0$ and $\rho > 0$), there is no APD alternans, and thus $\Delta a(x,t) = 0$, the Ca-SDA pattern can be any pattern determined by the initial condition.

3) When the APD subsystem is unstable and the Ca subsystem is stable ($\alpha > 0$ and $\rho < 0$), the Ca-SDA pattern passively follows the APD-SDA pattern.

4) When both subsystems are unstable ($\alpha > 0$ and $\rho > 0$), the Ca-SDA pattern can be dyssynchronous or synchronized to the APD-SDA pattern, which can be understood as follows. Under this condition, the steady-state Ca-SDA pattern is determined by the solutions of $f(\Delta c) = 0$, in which

$$f(\Delta c) = \rho\Delta c - \varepsilon\Delta c^3 + \sigma\Delta a \quad (12)$$

$f(\Delta c) = 0$ can exhibit either three real solutions or one real solution (Fig.4A), and the transition occurs when $|\sigma_c \Delta a| = \sqrt{\frac{4\rho^3}{27\varepsilon}}$ or in another form:

$$|\sigma_c| = \sqrt{\frac{4}{27}}\rho\frac{|\Delta c|}{|\Delta a|} = \sqrt{\frac{4\rho^3\beta}{27\varepsilon\alpha}} \quad (13)$$

in which $\Delta a = \pm\sqrt{\frac{\alpha}{\beta}}$ and $\Delta c = \pm\sqrt{\frac{\rho}{\varepsilon}}$ are the steady-state alternans amplitudes of a single cell. Note that Eq.13 is valid only for $\alpha > 0$ since $\Delta a = 0$ for $\alpha \leq 0$. When $|\sigma| > |\sigma_c|$, $f(\Delta c) = 0$ has one real solution, otherwise, there are three real solutions. When there are three solutions, Δc of a cell can be either the positive solution or the negative solution depending on the initial condition. Under this condition, the Ca-SDA pattern can be arbitrary, independent of the APD-SDA pattern and determined solely by the initial condition (left panel in Fig.4B). When there is only one solution, Δc follows the same sign of Δa, and thus the Ca-SDA pattern synchronizes to the APD-SDA pattern (right panel in Fig.4B). Note that in the nodal region, Δc still varies from cell to cell, which is due to that Δa is too small to synchronize Δc as indicated by Eq.13. Therefore, when $|\sigma| > |\sigma_c|$, synchronization of the Ca-SDA pattern to APD-SDA pattern occurs, except in the nodal region where $|\Delta a|$ is small.

In cardiac myocytes, stochastic opening of ion channels causes random fluctuations in both APD and Ca. However, due to the cell-to-cell coupling, the fluctuations in APD become small in cardiac tissue [72]. On the other hand, the random fluctuations in Ca can be very large [73-77] due to criticality [17, 78]. We hypothesize that the random noise can lower the threshold of synchronization, i.e., the noise in Ca can promote synchronization of $\Delta c(x,t)$ to $\Delta a(x,t)$. We demonstrate this by adding noise to the system. Since the random fluctuation in APD is small, we only add noise to Ca, i.e., we add noise to Eq.11 but not Eq.10. Furthermore, for simplicity, we add a Gaussian white noise to Eq.11, i.e.,

$$T\frac{d\Delta c}{dt} = \rho\Delta c - \varepsilon\Delta c^3 + \sigma\Delta a + \eta(t) \quad (14)$$

where $\eta(t)$ is the Gaussian white noise satisfying $<\eta(t)> = 0$ and $<\eta(t)\eta(t')>= 2D\delta(t-t')$. D is the noise strength. The corresponding Fokker-Planck equation describing the probability of Δc [$p(\Delta c)$] is: $\frac{\partial p}{\partial t} = -\frac{\partial f(\Delta c)p}{\partial \Delta c} + D\frac{\partial^2 p}{\partial \Delta c^2}$. The steady-state solution of the Fokker-Planck equation is expressed as [79]:

$$p(\Delta c) \propto \exp[-\frac{U(\Delta c)}{D}] \quad (15)$$

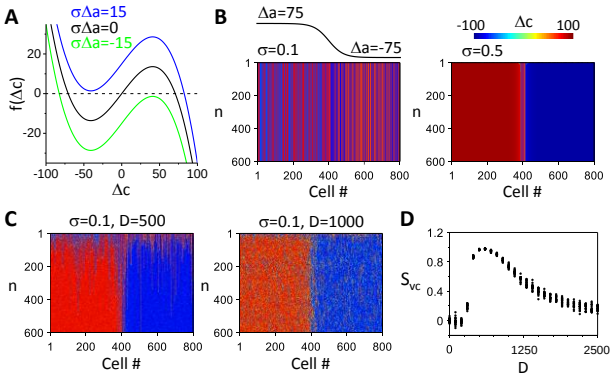

FIG.4. Synchronization of Ca-SDA to APD-SDA patterns in the AE model without Ca-to-APD coupling ($\gamma = 0$). A. Plots of function $f(\Delta c)$ (Eq.12) for different $\sigma\Delta a$ values. B. Space-time plots of Δc for $\sigma = 0.1$ (left) and $\sigma = 0.5$ (right) for a one-node APD-SDA as indicated. C. Space-time plots of Δc for $\sigma = 0.1$ with two noise strengths: $D = 500$ (left) and $D = 1000$ (right). D. S_{vc} vs noise strength D. For each D, 20 simulations with different random initial conditions are carried out with the corresponding S_{vc} plotted. In the simulations in B-D, the initial conditions for Ca-SDA are spatially random in which Δc is a binary number, randomly chosen as either -100 or 100. Δa is a one-node SDA as indicated in B. $\alpha = 0.5$ and $\rho = 0.5$.

in which $U(\Delta c) = -\frac{\rho}{2}\Delta c^2 + \frac{\varepsilon}{4}\Delta c^4 + \sigma \Delta a \Delta c$ is a double-well potential. When $\sigma \Delta a = 0$, the probability distribution is symmetric for the two potential wells. When $\sigma \Delta a \neq 0$, one potential well is higher than the other, which causes the transition of Δc from the higher potential well to the lower potential well, synchronizing the Ca-SDA pattern to the APD-SDA pattern. For example, for the case of $\sigma = 0.1$ in Fig.4B, adding noise causes the Ca-SDA pattern to synchronize to the one-node APD-SDA pattern (Fig.4C).

To quantify the degree of synchronization between the APD-SDA pattern and the Ca-SDA pattern, we define a synchronization index as follows:

$$S_{vc}(t) = \frac{1}{L}\sum_{i=1}^{L} sgn[\Delta a(i,t)] \times sgn[\Delta c(i,t)] \qquad (16)$$

where L is the length of the cable (the total number of cells). A perfectly synchronized Ca-SDA pattern with an APD-SDA pattern gives rise to $S_{vc} = 1$ for electromechanically concordant SDA and $S_{vc} = -1$ for electromechanically discordant SDA. Fig.4D plots S_{vc} versus the noise strength, showing that when the noise is weak, no synchronization occurs, but once the noise is strong enough, synchronization occurs. However, the synchronization weakens as the noise strength increases due to the increased probability of the transitions from the lower potential well to the higher one.

(b) $\gamma \neq 0$ *and* $\sigma = 0$. In this case, Ca is not affected by APD but APD is affected by Ca. This condition can be more easily satisfied in the real system. For example, this condition can be satisfied at slow pacing rates since the Ca channels, ryanodine receptors, and SR Ca load are all recovered before the next beat so that Ca is not affected by the change of APD in the previous beat. Under this condition, Eqs. 3 and 4 are then reduced to:

$$T\frac{\partial \Delta a}{\partial t} = \alpha \Delta a - \beta \Delta a^3 + \gamma \Delta c(x,t) + \xi^2 \frac{\partial^2 \Delta a}{\partial x^2} \qquad (17)$$

When the Ca subsystem is stable ($\rho < 0$), i.e., there is no Ca-driven alternans, then $\Delta c(x,t) = 0$, Eq.17 exhibits a front solution in an infinite spatial domain as [51]:

$$\Delta a(x,t) = \sqrt{\frac{\alpha}{\beta}}\tanh\left(\sqrt{\frac{\alpha}{2\xi^2}}x\right) \qquad (18)$$

In this case, the node dynamics is determined solely by voltage, predicted by $\lambda_{k,1}$, which has been investigated in detail in our previous analysis [51]. When the Ca subsystem is unstable ($\rho > 0$), Eq.17 cannot be solved analytically in general. We first consider a special case in which we assume that the Ca alternans is spatially concordant, i.e., $\Delta c(x,t) = \Delta c$ is a constant. Then Eq.17 has the following solution in an infinite spatial domain:

$$\Delta a(x,t) \propto \tanh\left[\sqrt{\frac{\alpha'}{2\xi^2}}(x - v(\gamma \Delta c)t)\right] \qquad (19)$$

in which $v(\gamma \Delta c)$ is the front (or node) velocity as a function of $\gamma \Delta c$. The velocity is positive if $\gamma \Delta c$ is positive or vice versa. This implies that if the Ca alternans is spatially concordant (i.e., Ca-SCA), an initial node in APD alternans will eventually drift off the tissue, resulting in an APD-SCA pattern. In other words, if Ca alternans is spatially concordant, APD alternans has to be spatially concordant.

However, when the Ca alternans is spatially discordant (i.e., Ca-SDA), the APD-SDA patterns are more complex, i.e., the APD-SDA can be either synchronized or desynchronized to the Ca-SDA pattern depending on the spatial scale of the Ca-SDA pattern and the coupling strength γ. As shown in our previous analysis [51], in homogeneous tissue without Ca-driven alternans, the APD-SDA node's stability is neutral. However, in the presence of Ca-driven alternans, the APD-SDA node in homogeneous tissue may become stable or anchored to the Ca-SDA node, as explained in Fig.5A. We assume a Ca-SDA pattern with a single node (red curve in Fig.5A). If the initial node of the APD-SDA is in the left of the Ca-SDA node, based on Eq.19, the APD-SDA node will drift toward the right since $\gamma \Delta c > 0$. If the initial APD-SDA node is in the right of the Ca-SDA node,

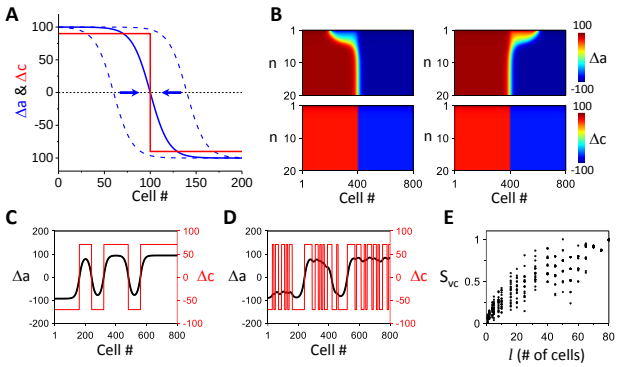

FIG.5. Synchronization of APD-SDA to Ca-SDA in the AE model without APD-to-Ca coupling ($\sigma = 0$). A. Schematic plot of synchronization of an APD-SDA (blue) to a Ca-SDA (red). Arrows indicate that an initial APD-SDA node away from the Ca-SDA node drifts toward the Ca-SDA node. B. Simulation of the AE model showing the scenarios in A. C. Synchronization of APD-SDA to a Ca-SDA pattern when the spatial scale of Ca-SDA pattern is large. D. Same as C but the spatial scale of Ca-SDA pattern is small. E. S_{vc} versus the spatial scale (l) of the Ca-SDA pattern. $\alpha = 0.5$, $\rho = 0.5$, and $\gamma = 0.5$. In the simulations in C-E, the initial conditions are spatially random SDAs in which Δa and Δc are binary numbers, randomly chosen as either -100 or 100 with spatial segmentation length l. $l = 80$ cells for C and $l = 10$ cells for D. In E, 20 random initial conditions are used for each l.

then it will drift toward the left since $\gamma \Delta c < 0$. The final APD-SDA state is that its node is completely aligned with the Ca-SDA node, synchronizing to the Ca-SDA pattern. The theoretical scenario is demonstrated in simulations of the AE model as an example shown in Fig.5B. However, the synchronization of the APD-SDA pattern to the Ca-SDA pattern depends on the coupling strength γ and the spatial scale of the Ca-SDA pattern, i.e., the size of the synchronized clusters in Ca-SDA pattern. When the spatial scale of the Ca-SDA pattern is large, APD-SDA synchronizes to the Ca-SDA (e.g., Fig.5C), but when the spatial scale is small, they do not synchronize (e.g., Fig.5D). Fig.5E plots S_{vc} versus the spatial scale of the given Ca-SDA patterns, showing that the degree of synchronization increases with the increase of the spatial scale of Ca-SDA.

The case shown in Fig.5 is for $\gamma > 0$, but the results still hold for $\gamma < 0$. The difference is that for $\gamma > 0$, the SDA patterns are electromechanically concordant, but for $\gamma < 0$, the SDA patterns are electromechanically discordant. Moreover, the results will also hold for periodic boundary conditions. Note that the number of nodes can be either even or odd under open boundary conditions, but it has to be even for periodic boundary conditions due to the required symmetry [i.e., Ca (or APD) has to be equal at the two boundaries]. Similar to the case of open boundary conditions, if there is no Ca-SDA, then the APD-SDA nodes are unstable, which will disappear by drifting toward each other and annihilate, leading to APD-SCA. When Ca alternans is discordant, then the APD-SDA will synchronize or desynchronize to the Ca-SDA the same ways as shown in Fig.5.

3. Synchronization of APD-SDA and Ca-SDA patterns when $\gamma\sigma > 0$

This condition is satisfied when $\gamma > 0$ and $\sigma > 0$ or $\gamma < 0$ and $\sigma < 0$. Since $\gamma\sigma > 0$, the eigenvalues in Eq.8 are always real. As $\lambda_k < 0$ changes to $\lambda_k > 0$, a pitchfork bifurcation occurs, leading to alternans. Fig.6A plots the stability boundaries ($\lambda_k = 0$ for the larger of the two eigenvalues of Eq.8) for different k values. The spatial modes are unstable ($\lambda_k > 0$) above (or to the right of) the boundaries. As k increases, the stability boundary moves upright ward, indicating that high spatial modes are more stable. As $k \to \infty$, the boundary becomes vertical at $\rho \to 0$, which indicates that for $\rho > 0$, all modes are unstable. Therefore, for $\rho < 0$, the number of nodes of a cable is largely determined by the mode stability as investigated in detail in our previous study [51]. For $\rho > 0$, i.e., the Ca subsystem is unstable, since all the linear modes are unstable, any pattern is possible. However, due to the coupling between cells and between APD and Ca, as well as nonlinear interactions, the spatial patterns cannot be completely arbitrary, which depend on the stabilities of the APD and Ca subsystems, the coupling strength, and the initial conditions.

Figs.6 B-E show some representative steady-state SDA patterns for the same set of α and ρ values ($\alpha = \rho = 0.5$). Figs. 6 B and C show a single-node and a high spatial periodicity SDA using spatially periodic initial conditions, respectively. As the number of nodes increases, the magnitudes of APD alternans are attenuated. Figs.6 D and E

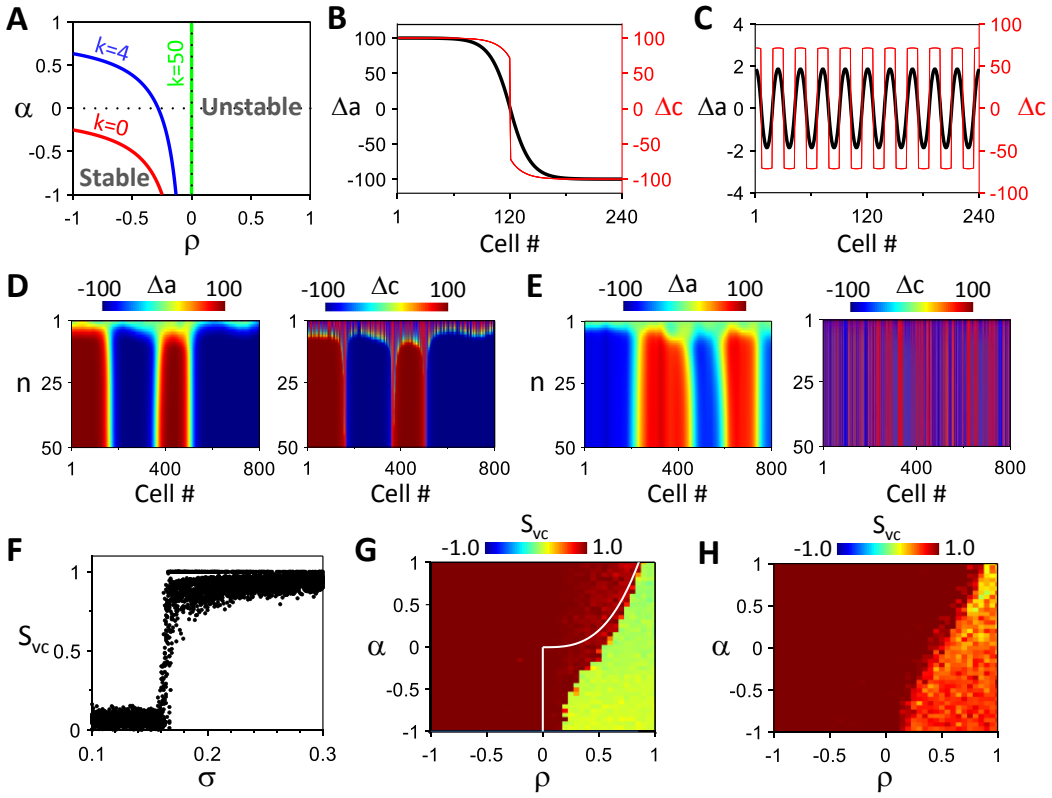

FIG.6. Spatiotemporal Ca and APD dynamics in the AE model for $\gamma\sigma > 0$. A. Stability boundaries (colored lines) in the ρ-α plane for different spatial modes of the linear stability analysis of the steady state. Shown are the boundary for $k = 0$ (red), 4 (blue), and 50 (green). $\gamma = 0.5$ and $\sigma = 0.5$. B. Steady-state Δa (black) and Δc (red) in space for beat #100 with 1 node in both Δa and Δc. C. Same as B but with 20 nodes in both Δa and Δc. D. Space-time plots of Δa and Δc with an initial condition of $\Delta a = 0$ and random Δc in which Δc is a binary number, uniformly chosen as either -100 or 100. $\gamma = 0.5$ and $\sigma = 0.5$. E. Same as D but with $\sigma = 0.1$. F. S_{vc} vs σ. For each σ, 20 S_{vc} values from different initial conditions as in C and D are plotted. $\gamma = 0.5$. G. Color map of S_{vc} vs α and ρ. For each set of α and ρ, one random initial condition (spatial scale $l = 1$ cell) is simulated. $\gamma = 0.5$ and $\sigma = 0.3$. The white line is the synchronization boundary predicted by Eq.13 under $\gamma = 0$, showing that positive Ca-to-APD coupling ($\gamma > 0$) enhances spontaneous synchronization. H. Same as G but with a larger spatial scale of the initial conditions: $l = 20$ cells.

show SDA from random initial conditions with strong and weak APD-to-Ca coupling, respectively. Under strong coupling, synchronous APD-SDA and Ca-SDA patterns form spontaneously although the initial conditions are purely random. When the coupling is weak, APD-SDA and Ca-SDA becomes dyssynchronous. The mechanisms of pattern formation and synchronization of the SDA patterns can be understood based on the simple cases of $\gamma = 0$ (Fig.4) and $\sigma = 0$ (Fig.5). An APD-SDA pattern forms first because of the heterogeneous initial condition and spatial mode instability, which then synchronizes the Ca-SDA pattern via the mechanism described in Fig.4. Once they are synchronized, the Ca-SDA pattern stabilizes the nodes via the mechanism described in Fig.5.

Fig.6F shows S_{vc} versus σ from simulations done the same way as in Figs. 6 D and E. Synchronization occurs when σ is greater than a certain value, as predicted by Eq.13. Note that Eq.13 is only valid for $\gamma = 0$, which predicts $\sigma_c = 0.192$ for the α and ρ values used. Since $\gamma > 0$ in Fig.6F, the σ value for synchronization is smaller, indicating that positive Ca-to-APD coupling enhances synchronization [see also the comparison of the boundary for $\gamma = 0$ (white line) with the boundary from the simulation for $\gamma > 0$ in Fig.6G]. As indicated by Eq.13, the synchronization of APD-SDA and Ca-SDA depends on α and ρ (Fig.6G), i.e., the stabilities of the voltage and Ca subsystems. When $\rho < 0$, i.e., the Ca subsystem is stable, Ca-SDA and APD-SDA are always synchronized. When $\rho > 0$, i.e., the Ca subsystem is unstable, spontaneous synchronization is promoted by increasing α and/or decreasing ρ. In other words, larger APD alternans and/or smaller Ca alternans potentiates synchronization, which is implied in Eq.13 ($|\sigma_c| \propto \frac{|\Delta c|}{|\Delta a|}$). In the region where spontaneous synchronization fails (green region in Fig.6G), synchronization can be enhanced by

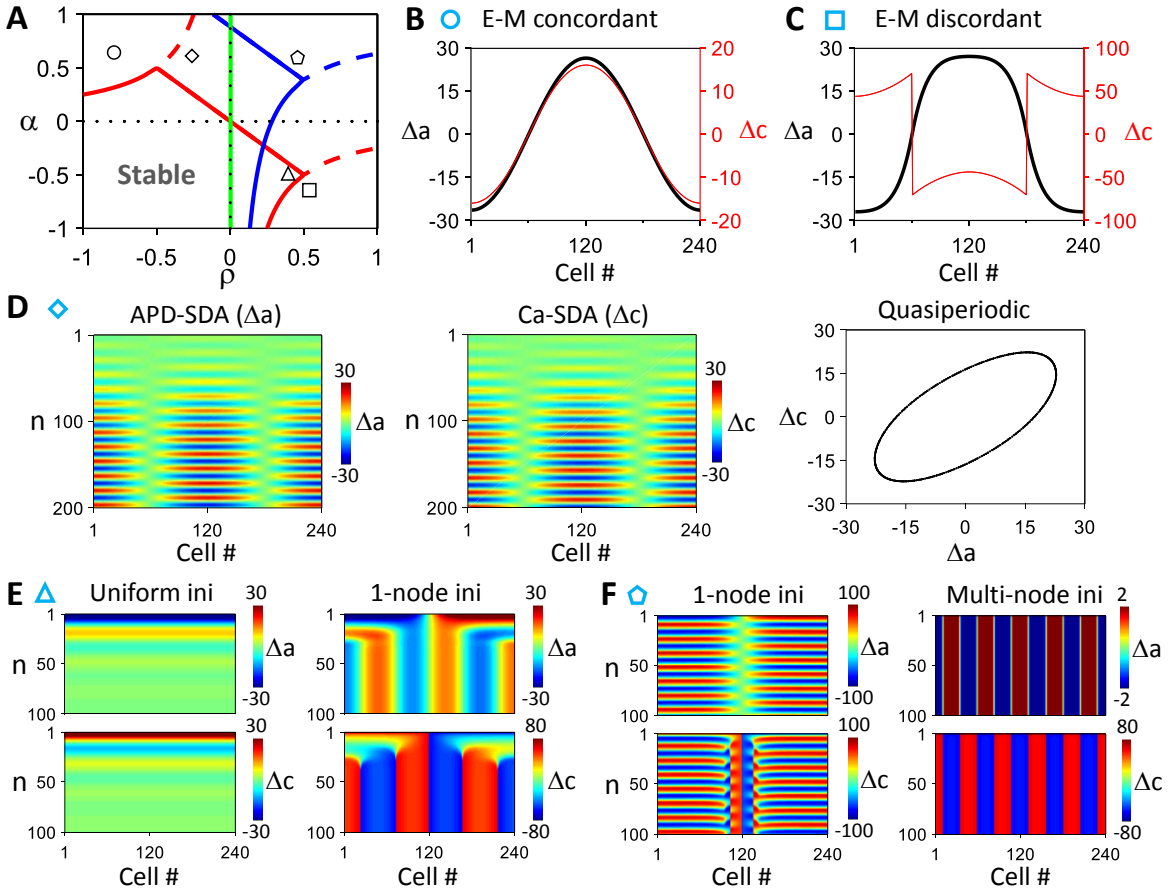

FIG.7. Spatiotemporal Ca and APD dynamics in the AE model for $\gamma\sigma < 0$. A. Stability boundaries (colored lines) in the ρ-α plane for different spatial modes of the linear stability analysis of the steady state. Shown are the boundaries for $k = 0$ (red), 4 (blue), and 50 (green). The spatial mode is stable inside (in the lower-left direction of) the solid lines. $\gamma = -0.5$ and $\sigma = 0.5$. B. Steady-state Δa (black) and Δc (red) showing an electromechanically concordant SDA in which Δa and Δc are in-phase. $\alpha = 0.6$ and $\rho = -0.8$, marked by the circle in A. C. Steady-state Δa (black) and Δc (red) showing an electromechanically discordant SDA in which Δa and Δc are anti-phase. $\alpha = -0.7$ and $\rho = 0.5$, marked by the square in A. D. Space-time color-scale plots of Δa (left) and Δc (middle) showing a quasiperiodic SDA in which Δa and Δc are not phase-locked but quasiperiodic (right). $\alpha = 0.6$ and $\rho = -0.3$, marked by the diamond in A. E. A uniform initial condition leads to a stable steady state (left, no alternans), but a non-uniform (one-node) initial condition leads to multi-node electromechanically discordant SDA (right). $\alpha = -0.5$ and $\rho = 0.4$, marked by the triangle in A. F. A one-node initial condition leads to a quasiperiodic SDA (left), but a multi-node initial condition leads to a multi-node electromechanically discordant SDA. $\alpha = 0.6$ and $\rho = 0.4$, marked by the pentagon in A. In E and F, the upper panels are color-scale plots of Δa, and the lower panels are those of Δc.

increasing the spatial scale of the initial Ca-SDA pattern (Fig.6H) via the mechanism as shown in Fig.5.

The same applies to the condition of $\sigma < 0$ and $\gamma < 0$ except that the SDA patterns are electromechanically discordant.

4. SDA dynamics when $\gamma\sigma < 0$

In this case, Ca-to-APD coupling is negative and APD-to-Ca coupling is positive ($\gamma < 0$ and $\sigma > 0$) or vice versa ($\gamma > 0$ and $\sigma < 0$). Since $\gamma\sigma < 0$, the eigenvalues in Eq.8 can be either real or a pair of complex conjugates, and thus the system can undergo a pitchfork bifurcation or a Hopf bifurcation. A pitchfork bifurcation leads to alternans and a Hopf bifurcation leads to quasiperiodic behavior. Fig.7A shows the stability boundaries in the α-ρ plane for different spatial modes (k values) of the steady state. The arc lines are the pitchfork bifurcations, and the straight ones are the Hopf bifurcations which are determined by $\rho = -(\alpha - \xi^2 k^2)$ and $\gamma\sigma < -(\alpha - \xi^2 k^2 - \rho)^2/4$. The stability boundary for $k = 0$ is the same as for the single cell, which has been investigated in the previous studies [21, 22]. It has been shown that the alternans can be electromechanically concordant in which APD and Ca alternate with their phases locked in-phase, electromechanically discordant in which APD and Ca alternate with their phases locked anti-phase, or electromechanically quasiperiodic in which APD and Ca alternate with their phases changing quasiperiodically.

Because of the complex cellular alternans dynamics, the spatiotemporal dynamics in tissue become more complex. Figs.7 B, C, and D show three characteristic SDA patterns: electromechanically concordant, discordant, and quasiperiodic alternans in the 1D cable. However, the stability boundary shifts upwards and leftwards as k increases, resulting in intersections of the stability boundaries for different k values. This differs from the $\gamma\sigma > 0$ case, in which there are no intersections of the stability boundaries for different k values. The interaction of the stability boundaries results in more complex dynamics in the cable. For example, in the location marked by the triangle in Fig.7A, it predicts that the uniform mode ($k = 0$) is stable, but a non-uniform mode is unstable. Examples of this case in Fig.7E in which the homogeneous solution is stable (no alternans) but inhomogeneous initial condition leads to a multiple-node and electromechanically discordant SDA. In the location marked by the black square, the low-k modes are quasiperiodic but the high-k modes are stable. Fig.7F shows an example in which a single-node (low-k mode) SDA is quasiperiodic, but a multiple-node (high-k mode) pattern is stable. If one uses random initial conditions with different spatial scales, patterns of a mixture of quasiperiodic and stable alternans can co-exist.

The results in Fig. 6 are for SDA dynamics versus α and ρ for positive coupling and those in Fig.7 are for negative coupling. Fig.8 shows S_{vc} in σ-γ plane for $\alpha = 0.5$ and $\rho = 0.5$ for which both the APD subsystem and the Ca subsystem are unstable. Fig.8A is the color map of S_{vc} for pure random initial conditions and Fig.8B is that for a larger spatial scale of the initial conditions. When $\gamma\sigma > 0$, APD-SDA and Ca-SDA are synchronized when $|\sigma| > |\sigma_c|$, and the SDA patterns are electromechanically discordant when $\gamma < 0$ (lower-left quadral, $S_{vc} \approx -1$) and electromechanically concordant when $\gamma > 0$ (upper-right quadral, $S_{vc} \approx 1$). When $\gamma\sigma < 0$, APD-SDA and Ca-SDA are synchronized but in quasiperiodic modes when $|\sigma| > |\sigma_c|$. Because of this, S_{vc} map (calculated at the last pacing beat) looks random since the APD-SDA and Ca-SDA are in different

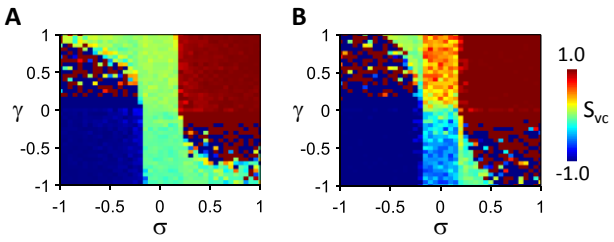

FIG.8. Color maps of S_{vc} versus σ and γ in the AE model. A. Purely random initial conditions of Δa and Δc (spatial scale $l = 1$ cell). B. Random initial conditions with a spatial scale of $l = 20$ cells. $\alpha = 0.5$ and $\rho = 0.5$. Note that in the upper-left and lower-right quadrals, $\gamma\sigma < 0$, the SDA dynamics is quasiperiodic, S_{vc} measured at the last beat depends on the status the SDA pattern, which varies from beat to beat. Therefore, the S_{vc} values in these two quadrals exhibit a random-like pattern in the color map. In the upper-right (electromechanically concordant) and lower-left (electromechanically discordant) quadrals, the SDA patterns are phase-locked and stable.

phases of quasiperiodicity at the last beat for different parameter sets. When $|\sigma| < |\sigma_c|$, APD alternans exhibits no effects on Ca alternans, the synchrony between APD-SDA and Ca-SDA is poor. In this region, the synchrony is enhanced by increasing the spatial scale of the initial condition (Fig.8B), via the mechanism of synchronization (due to APD-to-Ca coupling) shown in Fig.5.

In summary, the AE model demonstrates that there are two ways in which the APD-SDA and Ca-SDA patterns can be synchronized. The first one is spontaneous synchronization caused by strong APD-to-Ca coupling. In this mechanism of synchronization, the SDA patterns are selected by the APD-SDA patterns which are determined by the spatial mode instability and the initial conditions. This mechanism of synchronization is promoted by strong APD instability. The second one is initial condition dependent synchronization in which synchronization is promoted by increasing the spatial scale of the initial Ca-SDA patterns. This mechanism of synchronization is promoted by strong Ca instability. Once the system is synchronized, the APD-SDA and Ca-SDA may be locked into electromechanically concordant, discordant, and quasiperiodic patterns depending on the coupling relationships.

B. SDA dynamics in the 1D CML model

To examine the theoretical predictions of the AE model under more physiological conditions, we use a CML model formulated based on previous studies [51, 80], described in detail in the Appendix. This model contains physiological

parameters, such as APD restitution, fractional Ca release, and Ca release restitution, allowing us to directly link the dynamics to physiological parameters. We vary the following parameters: the slope of the APD restitution (controlled by τ_a in Eq.A6), the slope of the fractional release (controlled by β in Eq.A7), and the APD and Ca coupling strengths γ and σ_R (see Eqs. A1 and A9). Note that σ_R determines the APD-to-Ca coupling in the CML model, which is equivalent to σ in the AE model but not identical since σ_R affects the stability of Ca in the CML model. As shown in Eq.A9 [$q(d_n) = 1 - \sigma_R e^{-d_n/\tau_q}$], the APD-to-Ca coupling becomes weaker as the pacing period T is longer. When T is very long (and thus d_n is very large), $q(d_n) \to 1$, APD-to-Ca coupling vanishes. Therefore, at slow pacing, changing APD (and thus DI) has little or no effect on Ca release, which corresponds to $\gamma\sigma \approx 0$ in the AE model. However, as the pacing period T decreases (d_n becomes smaller), the term $\sigma_R e^{-d_n/\tau_q}$ has a bigger effect, and thus enhancing the APD-to-Ca coupling. In the CML model, the APD-to-Ca coupling is always positive since lengthening APD shortens DI resulting in a smaller $q(d_n)$ and thus a smaller Ca (see the definition of positive APD-to-Ca coupling in Fig.2C). Therefore, the sign of γ determines the coupling between APD and Ca.

For $\gamma > 0$, the coupling is positive, corresponding to $\gamma\sigma > 0$ in the AE model. Fig.9A shows the stability boundary in the τ_a-β plane for the single cell (or $k = 0$ mode) for $\gamma = 0.002$. The system is stable (no alternans) when both τ_a and β are large. Figs.9 B and C show two spatial patterns of alternans with a single node and multiple nodes, respectively. Figs. 9 D and E show SDA patterns from random initial conditions with strong and weak coupling, respectively. The APD-SDA and Ca-SDA are synchronized (except in the nodal region) when the APD-to-Ca coupling is strong (Fig.9D) but not when the coupling is weak (Fig.9E). The case in Fig.9D is similar to that in Fig.6D, in which the APD-SDA forms first and then synchronizes the Ca-SDA pattern to it. Figs.9 F and G show S_{vc} versus σ_R and S_{vc} versus T, respectively. Synchronization occurs when σ_R is greater than a critical value, agreeing with the AE model (Fig.6). The dependence of synchronization on T is more complex. S_{vc} is low for $T < 250$ ms, high for $250 < T < 285$ ms, low again for $285 < T < 320$ ms, and finally high for $T > 320$ ms. This can be understood based on the insights for AE model as follows. Based on Eq.13, $|\sigma_c| \propto \frac{|\Delta c|}{|\Delta a|}$, and thus synchronization tends to occur when Δc is small and Δa is large for a fixed σ. For $T < 250$ ms, Δa is relatively small but Δc is larger

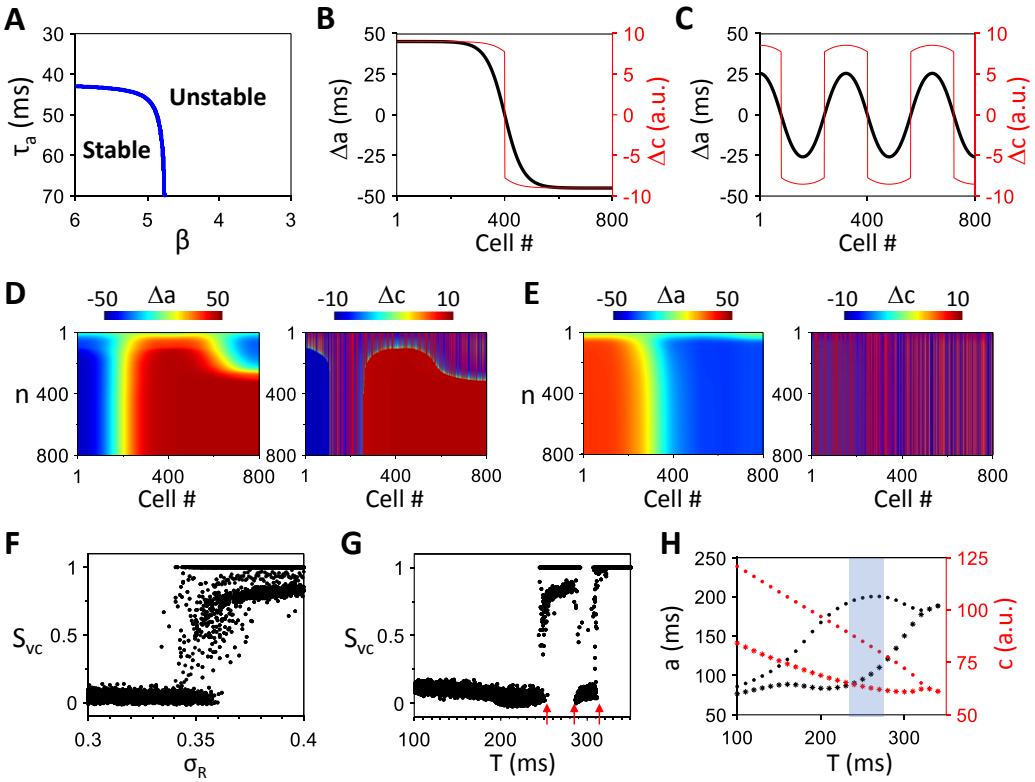

FIG.9. Spatiotemporal Ca and APD dynamics in the CML model for $\gamma > 0$. A. Stability boundary in the τ_a-β plane for $k = 0$ (or a single cell). B. Δa and Δc versus cell # recorded from beat #999 and #1000 with a single node. C. Same as B but with multiple nodes. D. Δa and Δc versus n with a random initial condition. E. Same as D but with a weaker coupling, $\sigma_R = 0.3$. F. S_{vc} versus σ_R. 20 different random initial conditions are used for each σ_R. G. S_{vc} versus T. 20 random initial conditions are used for each T. Arrows mark the T for the transition between desynchronized and synchronized SDA patterns. In F and G, the cases of $S_{vc} = 1$ correspond to SCA. H. a and c versus T for a single cell. The default parameters are: $T = 270$ ms, $\tau_a = 40$, $\beta = 4$, $\gamma = 0.002$, and $\sigma_R = 0.4$.

(Fig.9H), and thus the ability of APD-SDA to synchronize Ca-SDA is not strong enough. But as T increases, Δa increases while Δc decreases, and when T is large enough (shaded region in Fig.9H), Δa is large enough to synchronize Δc, causing spontaneous synchronization. As T increases further, Δa decreases again, which may be too small to synchronize Δc. As $T > 320$ ms, both APD and Ca 0 : the electromechanically concordant, discordant, and quasiperiodic alternans regions, which are marked by different colors. Figs.10 B-F show steady-state patterns or space-time plots for different initial conditions and different parameter sets marked by the symbols in Fig.10A. The behaviors are almost identical to those predicted by the AE model shown in Fig.7.

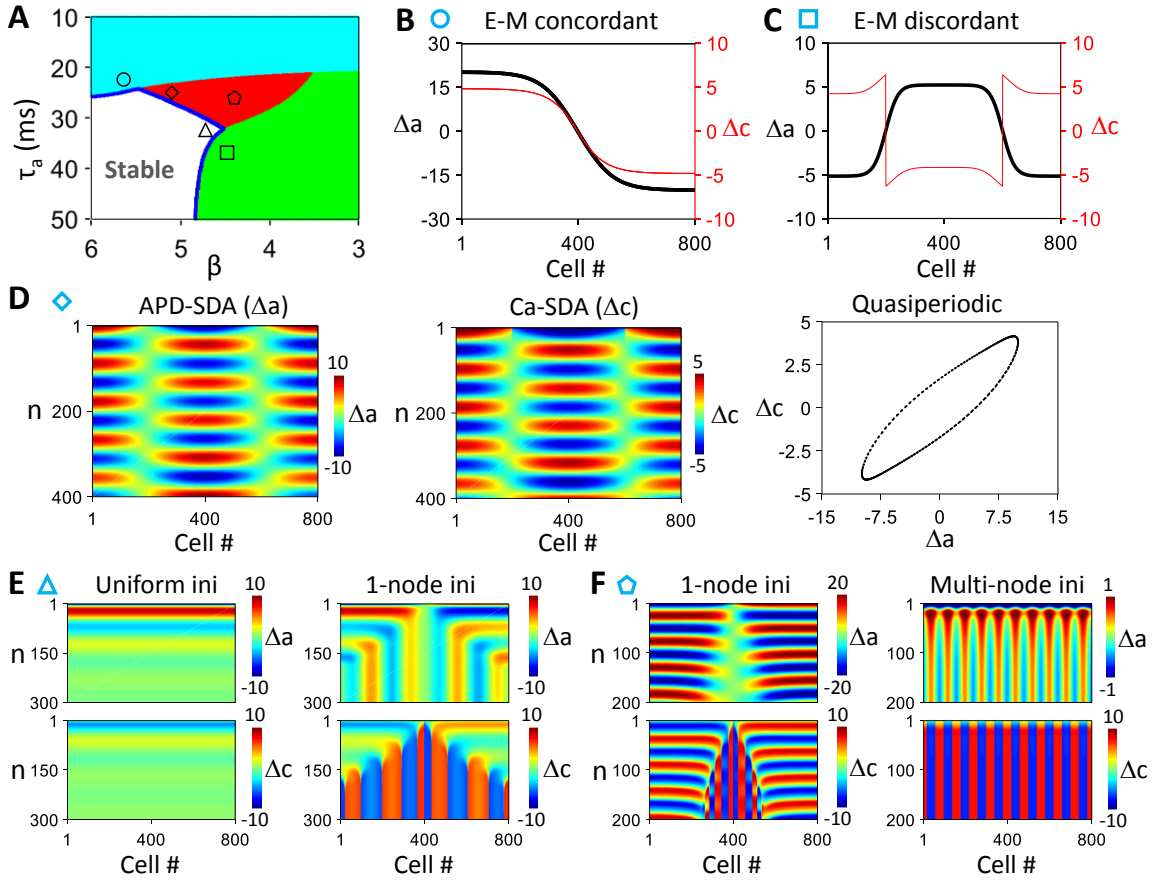

FIG.10. Spatiotemporal Ca and APD dynamics in the CML model for $\gamma < 0$. A. Phase diagram showing different Ca and APD dynamics versus τ_a and β in a single cell. White: Stable steady state; Cyan: Electromechanically concordant alternans; Green: Electromechanically discordant alternans; and Red: Quasiperiodicity. $\gamma = -0.002$, $\sigma_R = 0.8$, and $T = 250$ ms. B. Steady-state Δa (black) and Δc (red) showing an electromechanically concordant SDA. $\tau_a = 24$ and $\beta = 5.7$, marked by the circle in A. C. Steady-state Δa (black) and Δc (red) showing an electromechanically discordant SDA. $\tau_a = 38$ and $\beta = 4.6$, marked by the square in A. D. Space-time color-scale plots of Δa (left) and Δc (middle) showing a quasiperiodic SDA (right). $\tau_a = 24$ and $\beta = 5.3$, marked by the diamond in A. E. A uniform initial condition leads to a stable steady state (left, no alternans), but a non-uniform (1-node) initial condition leads to multi-node electromechanically discordant SDA (right). $\tau_a = 32$ and $\beta = 4.6$, marked by the triangle in A. F. A 1-node initial condition leads to a quasiperiodic SDA (left), but a multi-node initial condition leads to a multi-node electromechanically discordant SDA. $\tau_a = 27$ and $\beta = 4.5$, marked by the pentagon in A. In E and F, the upper panels are color-scale plots of Δa, and the lower panels are those of Δc

are stable, the system always synchronizes. Note that as in the AE model, when σ_R is small (or T is short), spontaneous synchronization fails, but the APD-SDA and Ca-SDA patterns can still be synchronized if the spatial scale of the initial Ca-SDA pattern is large.

For $\gamma < 0$, the coupling is negative. Fig.10A shows the stability boundary in the τ_a-β plane for the single cell (or the $k = 0$ mode) for $\gamma = -0.002$. Unlike in the AE model that one can calculate the stability boundaries easily for any k, it becomes nontrivial for the CML model. We numerically determine the three regions of alternans behaviors for $k =$

C. SDA dynamics in a 1D cable of the rabbit ventricular myocyte model

To further examine the theoretical predictions in physiologically detailed ionic models, we carry out 1D cable simulations using the rabbit ventricular myocyte model by Mahajan et al [61]. Fig.11A is a bifurcation diagram showing APD and peak Ca versus pacing period T. Alternans occurs when $T < 230$ ms. Figs.11 B-F show different SDA patterns resulted from different initial conditions for $T =$ 180 ms. In Figs.11 B and C, the initial conditions are

periodic. In Figs. 11 D-F, the initial conditions are random with different spatial scales. In the cases of random SDA patterns, the Ca-SDA and APD-SDA patterns are synchronized when the spatial scale is large but become dyssynchronous when it is small. These features are the same

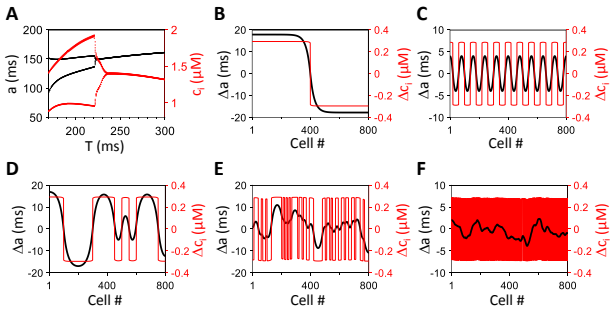

FIG.11. APD-SDA and Ca-SDA patterns in a 1D cable of the rabbit ventricular cell model. A. Bifurcation diagrams showing a and peak c_i versus the pacing period T. B-F. Steady-state APD-SDA and Ca-SDA patterns for different initial conditions. The spatial scales of random initial conditions in D-F are $l = 50$ cells, $l = 10$ cells, and $l = 1$ cell, respectively. $T = 180$ ms. Random initiation conditions are set by random initial values of the SR Ca load.

as for the AE and the CML model. Since the APD and Ca coupling is positive, we do not observe electromechanically discordant and quasiperiodic SDA patterns in this ionic model. We also do not observe spontaneous synchronization with pure random initial conditions, indicating that the voltage-driven instability in this model is either absent or not strong enough to promote spontaneous synchronization. The instability leading to alternans in the model is mainly Ca-driven.

D. Nodal line dynamics and SDA pattern synchronization in 2D tissue models

SDA nodes form nodal lines in 2D tissue. When the nodal lines are straight, they behave the same way as the SDA nodes in 1D cable. However, nodal lines can become curved in 2D tissue (such as the ones shown in Fig.1), and a question arising is how the curvature affects the stability of the nodal lines and the SDA dynamics. As shown in our previous studies [50, 51], in the absence of Ca alternans, the SDA nodes or nodal lines are marginally stable in homogeneous tissue. Curved nodal lines or nodal rings are unstable, which become straight or shrink and disappear unless the tissue is heterogeneous. Here we investigate the effects of nodal line curvature on nodal line stability and synchronization of SDA patterns in 2D homogeneous tissue in the presence of Ca alternans. We extend the AE model into 2D tissue as:

$$T\frac{\partial \Delta a}{\partial t} = \alpha\Delta a - \beta\Delta a^3 + \gamma\Delta c + \xi^2\left(\frac{\partial^2 \Delta a}{\partial x^2} + \frac{\partial^2 \Delta a}{\partial y^2}\right) \quad (20)$$

$$T\frac{\partial \Delta c}{\partial t} = \rho\Delta c - \varepsilon\Delta c^3 + \sigma\Delta a \quad (21)$$

First, we consider the stability of a nodal ring, and for the purpose of theoretical argument, we consider a special case in which there is no APD-to-Ca coupling ($\sigma = 0$). We further simplify the condition by assuming that the Ca alternans is spatially concordant and in steady state, i.e., $\Delta c(x, y, t) = \Delta c$. We transform Eq.20 into a polar coordinate system, which becomes:

$$T\frac{\partial \Delta a}{\partial t} = \alpha\Delta a - \beta\Delta a^3 + \gamma\Delta c + \frac{\xi^2}{r}\frac{\partial \Delta a}{\partial r} + \xi^2\frac{\partial^2 \Delta a}{\partial r^2} \quad (22)$$

$$T\frac{\partial \Delta c}{\partial t} = \rho\Delta c - \varepsilon\Delta c^3 \quad (23)$$

Assuming an initial APD-SDA nodal ring of radius r, one can obtain an eikonal-curvature equation for the node speed as [51]:

$$c_{node} = \frac{v(\gamma\Delta c)}{T} - \frac{\xi^2}{Tr} \quad (24)$$

where c_{node} is the velocity of the APD-SDA node, and the first term is caused by Ca-to-APD coupling and the second term by curvature. The sign of $v(\gamma\Delta c)$ depends on the sign of $\gamma\Delta c$. If $v(\gamma\Delta c) < 0$, the effect of Ca-to-APD coupling and that of curvature are in synergy. If $v(\gamma\Delta c) > 0$, the two effects compete, and there is a critical radius at which $c_{node} = 0$, which gives rise to,

$$r_c = \frac{\xi^2}{v(\gamma\Delta c)} \quad (25)$$

In other words, the drifting direction of the nodal ring depends on its radius. Now we consider that there is a nodal ring in Ca alternans. As depicted in Fig.12A, $v(\gamma\Delta c)$ is positive on one side and negative on the other side of the node. Therefore, if the initial APD nodal ring is outside the Ca nodal ring, the "force" from the curvature and the one from the Ca alternans are in synergy, pulling the APD-SDA nodal ring toward the Ca-SDA nodal ring. If the initial APD nodal ring is smaller than the Ca nodal ring, then the two forces compete with each other. Therefore, depending on the strength of the two forces, the APD-SDA nodal ring can

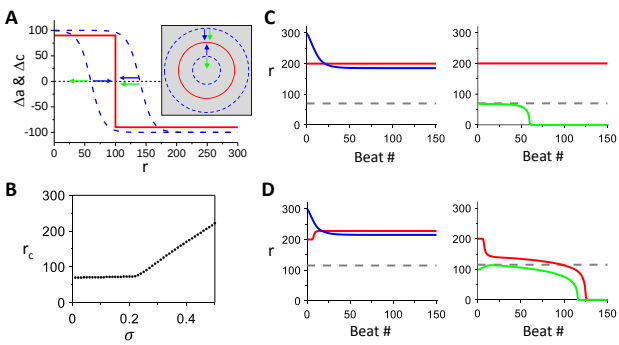

FIG.12. APD-SDA and Ca-SDA nodal ring dynamics in 2D tissue of the AE model. A. Schematic plots to illustrate the effects of Ca-SDA nodal ring (red) and curvature on APD-SDA nodal ring (dashed blues). The blue arrows indicate the "force" of the Ca-SDA nodal ring and the green arrows indicate the "force" of the curvature on the APD-SDA ring. B. The critical ring radius (r_c) versus σ determined via computer simulations of the AE model (Eqs. 20 and 21). $\alpha = 0.5$, $\rho = 0.5$, and $\gamma = 0.1$. C. Ring radius r versus beat # for different initial ring radius for $\sigma = 0.1$. Left: the initial APD-SDA nodal ring (blue) radius $r > r_c$. Right: the initial APD-SDA nodal ring (green) radius $r < r_c$. D. Ring radius R versus beat # for different initial ring radius for $\sigma = 0.3$. Left: the initial APD-SDA nodal ring (blue) radius $r > r_c$. Right: the initial APD-SDA nodal ring (green) radius $r < r_c$.

either expand to move toward the Ca-SDA nodal ring and stabilizes, or shrink to disappear. Based on Eq.24, when the APD-SDA nodal ring radius is larger than r_c, it will synchronize to the Ca-SDA nodal ring as long as the Ca-SDA nodal ring is larger than r_c. When the APD-SDA nodal ring radius is smaller than r_c, it will shrink and disappear no matter what the Ca-SDA nodal ring radius is. However, in the presence of APD-to-Ca coupling ($\sigma \neq 0$), the nodal ring dynamics becomes more complex, which is demonstrated in the AE model and the ionic model below.

To verify the theoretical argument, we carry out numerical simulations of the AE model (Eqs. 20 and 21).

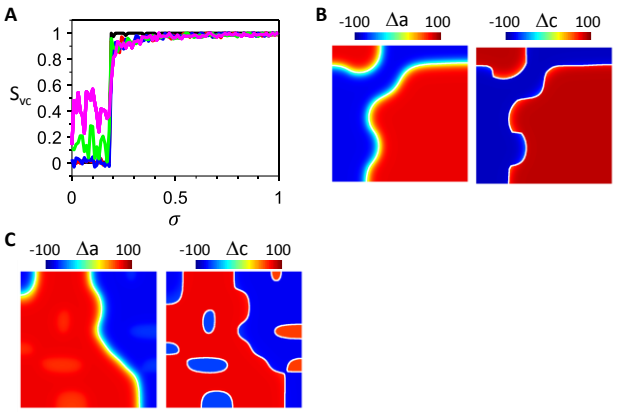

FIG.13. Synchronization of APD-SDA and Ca-SDA patterns when both APD and Ca are unstable. Simulations are done in the AE model with $\alpha = 0.5$, $\rho = 0.5$, and $\gamma = 0.1$. Tissue size is 800×800 cells. A. S_{vc} versus σ for different spatial scales of the initial condition with random block sizes: 1×1 cell (black), 10×10 cells (red), 20×20 cells (blue), 50×50 cells (green), and 100×100 cells (magenta). Note: Only one random initial condition is used for each σ for the calculation of S_{vc}. When $\sigma < \sigma_c \approx 0.19$, S_{vc} depends strongly on the block size of the initial condition. B. Example APD-SDA (left) and Ca-SDA (right) patterns for $\sigma = 0.3$. The initial condition block size is 100×100 cells. The calculated synchronization index is $S_{vc} = 0.93$. C. Example APD-SDA (left) and Ca-SDA (right) patterns for $\sigma = 0.1$. The initial condition block size is 100×100 cells. The calculated synchronization index is $S_{vc} = 0.75$. In B-C, the white lines are the nodal lines ($\Delta a = 0$ or $\Delta c = 0$).

Fig.12B shows r_c versus σ obtained from the simulations. r_c remains unchanged for $\sigma < 0.19$ but then increases almost linearly with σ. When σ is smaller than the critical value, the APD-SDA nodal ring synchronizes with the Ca-SDA nodal ring as long as both ring radius is greater than r_c or disappears when either the APD-SDA nodal ring radius or the Ca-SDA nodal ring radius is smaller than r_c (Fig.12C). The Ca-SDA nodal ring can be any size larger than the critical size and remains unchanged in time. These behaviors are the same as predicted by the simplified condition (Fig.12A). When σ is greater than the critical value, APD-SDA and Ca-SDA nodal rings will synchronize if their radii are greater than r_c, but the final ring radius depends on the initial ring sizes and the coupling strength. When either of their radii is smaller than r_c, both nodal rings disappear (Fig.12D). Note that the critical σ value is the same as the one when Ca-SDA is synchronized to APD-SDA via APD-to-Ca coupling, which is determined by Eq.13. Inserting $\alpha = 0.5$, $\beta = 0.0001$, $\rho = 0.5$, and $\varepsilon = 0.0001$ into Eq.13, one obtains $\sigma_c = 0.192$, agreeing with the simulation results.

To further investigate the synchronization of APD-SDA and Ca-SDA patterns in 2D tissue, we carry out simulations of the AE model using random initial conditions with different block sizes of both Δa and Δc. Fig.13A shows S_{vc} versus σ for different spatial scales of the initial SDA pattern. When $\sigma > 0.19$, APD-SDA and Ca-SDA become synchronized ($S_{vc} \approx 1$), almost independent of the spatial scales of the initial pattern. Fig.13B shows an example of the synchronized SDA patterns in which the APD-SDA nodal lines and Ca-SDA nodal lines co-localize and the nodal lines are stable and curved. Under this condition, no small nodal rings can exist, as predicted by the nodal ring results in Fig.12. When $\sigma < 0.19$, APD-SDA and Ca-SDA are either completely desynchronized ($S_{vc} \approx 0$) or partially synchronized ($0 < S_{vc} < 1$). The degree of synchrony is better (S_{vc} is larger) for a larger spatial scale of the initial SDA pattern. Fig.13C shows an example of a SDA pattern, in which the APD-SDA nodal lines co-localize with Ca-SDA nodal lines but there are several other Ca-SDA nodal rings without corresponding APD-SDA nodal rings. This behavior is the same as in the rabbit heart experiments shown in Fig.1.

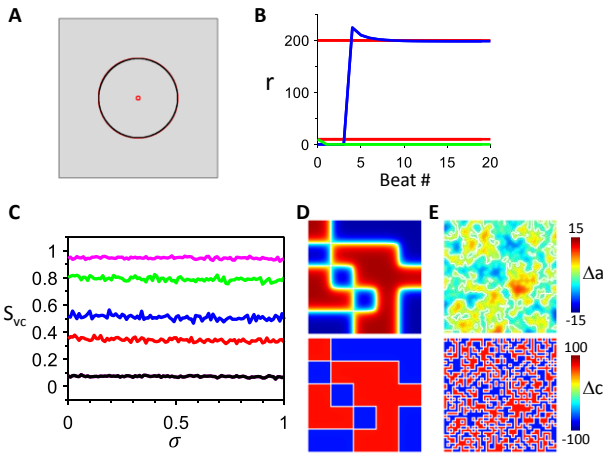

FIG.14. APD-SDA and Ca-SDA dynamics in 2D tissue when alternans is driven by Ca alone. Simulations are done in the AE model with $\alpha = -0.5$, $\rho = 0.5$, and $\gamma = 0.1$. Tissue size is 800×800 cells. A. Steady-state APD-SDA (black) and Ca-SDA (red) nodal rings. $\sigma = 0.1$. B. Ring radius versus beat # showing the time evolution for the APD-SDA (blue and green) and Ca-SDA (red) nodal rings shown in A. C. S_{vc} versus σ for different spatial scales of the random initial condition. Block sizes: 1×1 cell (black), 10×10 cells (red), 20×20 cells (blue), 50×50 cells (green), and 100×100 cells (magenta). D. Example APD-SDA (upper) and Ca-SDA (lower) patterns for $\sigma = 0.1$. The initial condition block size is 160×160 cells. The calculated synchronization index is $S_{vc} = 0.99$. E. Example APD-SDA (upper) and Ca-SDA (lower) patterns for $\sigma = 0.1$. The initial condition block size is 20×20 cells. The calculated synchronization index is $S_{vc} = 0.54$. In D and E, the white lines are the nodal lines ($\Delta a = 0$ or $\Delta c = 0$).

The results shown in Figs. 12 and 13 are for the condition in which both APD and Ca are unstable. If we use $\alpha = -0.5$ and $\rho = 0.5$ for which the APD subsystem is stable and the Ca subsystem is unstable, then the nodal ring dynamics and APD-SDA and Ca-SDA synchronization differ from the case in Figs.12 and 13. Figs.14 A and B show the results in which two Ca-SDA nodal rings are set initially, but only one APD-SDA nodal ring can exist, which co-localizes with the large Ca-SDA nodal ring. This behavior is independent of the APD-to-Ca coupling strength. Fig.14C shows S_{vc} versus σ for different spatial scales of the initial SDA pattern, showing that the synchrony does not depend on σ but only on the spatial scale of the initial condition. Figs. 14 D and E show two examples of the SDA patterns resulted from two initial conditions, respectively. For the large spatial scale (Fig.14D), the APD-SDA and Ca-SDA patterns are well synchronized. For the small spatial scale (Fig.14E), however, the synchrony is much reduced due to that there are very small spatial scales in the Ca-SDA pattern but not in the APD-SDA pattern due to cell-to-cell coupling.

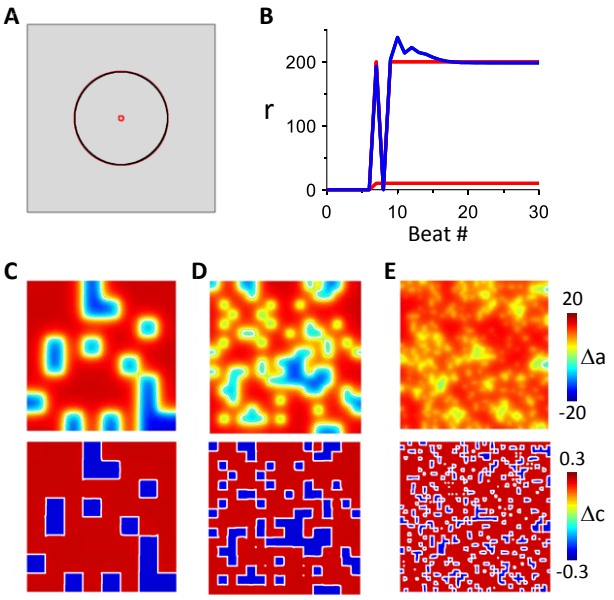

FIG.15. APD-SDA and Ca-SDA dynamics in a 2D tissue of the rabbit ventricular cell model. Tissue size is 800×800 cells and $T =$ 180 ms. A. Steady-state APD-SDA (black) and Ca-SDA (red) nodal rings. B. Ring radius versus beat # showing the time evolution of the APD-SDA (blue) and Ca-SDA (red) nodal rings. C. Example APD-SDA (upper) and Ca-SDA (lower) patterns. The initial condition block size is 100×100 cells. The calculated synchronization index is $S_{vc} = 0.93$. D. Example APD-SDA (upper) and Ca-SDA (lower) patterns. The initial condition block size is 50×50 cells. The calculated synchronization index is $S_{vc} =$ 0.76. E. Example APD-SDA (upper) and Ca-SDA (lower) patterns. The initial condition block size is 20×20 cells. The calculated synchronization index is $S_{vc} = 0.66$. In C-E, the white lines are the nodal lines ($\Delta a = 0$ or $\Delta c = 0$). Random initiation conditions are set by the random initial values of the SR Ca load and the gating variable of I_{Ks}.

We then carry out simulations of 2D tissue using the rabbit ventricular myocyte model. Figs.15 A and B show the nodal ring behavior, which is identical to that shown in Fig.14. Figs. 15 C-E show example SDA patterns resulted from random initial patterns of different spatial scales. Agreeing completely with those shown in Fig.14, i.e., synchronization occurs when the spatial scales are large but not for the small ones. Moreover, the SDA patterns always remain as the same as the initial Ca-SDA patterns (Note that in Figs. 14 and 15, the Ca-SDA patterns are composed of discretized square boxes that are the same as their initial conditions, while the APD-SDA patterns are smoothed due to cell-to-cell coupling). Agreeing with the 1D cable results in Fig.11, the 2D results in Fig.15 implies that in the rabbit ventricular myocyte model, alternans is mainly caused by the Ca-driven instability.

IV. Summary and Discussion

In this study, we investigate the mechanisms of formation and stability of the SDA dynamics and synchronization of APD-SDA and Ca-SDA patterns in cardiac tissue models in the presence of both voltage-driven and Ca-driven instabilities and the effects of Ca and voltage coupling. We show that when the Ca subsystem is stable, the Ca-SDA pattern always follows the APD-SDA pattern and thus they are always synchronized. When the Ca subsystem is unstable, synchronization of APD-SDA and Ca-SDA patterns depends on the stabilities of both subsystems, their coupling strengths, and the spatial scales of the initial Ca-SDA patterns. Spontaneous (initial condition-independent) synchronization is promoted by enhancing APD instability and reducing Ca instability as well as stronger Ca-to-APD and APD-to-Ca coupling, a pattern formation caused by dynamical instabilities. When Ca is more unstable and APD is less unstable or APD-to-Ca coupling is weak, synchronization of APD-SDA and Ca-SDA patterns is promoted by larger initially synchronized Ca-SDA clusters, i.e., initial condition-dependent synchronization. The synchronized APD-SDA and Ca-SDA patterns can be locked in-phase, anti-phase, or quasiperiodic depending on the coupling relationship between APD and Ca. Unlike the case of absence of Ca-driven instability in which curved nodal lines are unstable [50, 51], curved nodal lines can be stable in homogeneous tissue when Ca-driven alternans exists.

The theoretical and simulation results provide mechanistic insights into APD-SDA and Ca-SDA dynamics observed in experimental studies. Based on our theoretical insights that when there is no Ca-driven instability, the APD-SDA and Ca-SDA patterns are always synchronized. One can imply that Ca is unstable in those experimental settings [44, 48, 49] in which Ca-SDA and APD-SDA patterns are desynchronized (e.g., Fig.1). Moreover, the large spatial scales in the Ca-SDA pattern desynchronize with the APD-SDA pattern in these experiments indicate that the Ca and voltage subsystems may be both unstable (see Fig.13), since when either of the two subsystems is stable, APD-SDA and Ca-SDA will tend to be synchronized when the spatial scale

of the synchronized clusters of Ca-SDA pattern is large (Figs.14 and 15).

The mechanistic insights from the current study provide a better understanding of the roles of Ca-driven alternans in cardiac arrhythmogenesis. Since Ca in neighboring cells are not directly coupled, theoretically, their phases of alternans can be arbitrary from cell to cell. If alternans is caused solely by the Ca instability and the phases of Ca alternans are arbitrary, due to the smoothing effect caused by diffusive coupling of voltage, the amplitudes of APD alternans will be small. This cannot generate a large enough APD gradient for arrhythmogenesis [56]. Synchronization of the Ca alternans between cells is required to generate large amplitude APD-SDA for arrhythmogenesis. As shown in this study, there are two ways to synchronize the SDA patterns. The first one is when Ca alternates in phase in large clusters, which can synchronize APD-SDA to the Ca-SDA to generate large APD gradients (e.g., Figs. 5C and 11D). This type of clustering may naturally occur in the real system, for example, in heterogeneous tissue in which the onset of alternans is regionally heterogeneous [81, 82]. The second way is when APD-to-Ca coupling is strong enough so that APD-SDA and Ca-SDA are spontaneously synchronized to form SDA patterns with large alternans amplitude (e.g., Figs.6D and 9D). Strong APD-to-Ca coupling can be caused by Ca release restitution [67-69] [$q(d_n)$ in the CML model], which is promoted by fast heart rates. Therefore, Ca alternans at fast heart rates can be more arrhythmogenic than the one at slow heart rates due to stronger APD-to-Ca coupling promoted Ca-SDA and APD-SDA synchronization. In other words, fast heart rates not only promote Ca alternans but also promote Ca-SDA and APD-SDA synchronization to promote arrhythmias.

There are some limitations of this study needed to be mentioned. In the iterated map model, Ca alternans is caused by steep fractional release and APD alternans caused by steep APD restitution. Other mechanisms of Ca alternans and APD alternans exist [83, 84], which may affect the SDA dynamics. However, since the AE model is a generic model irrespective of the specific mechanisms of alternans, the mechanisms from AE model should still be applicable to the SDA dynamics from other mechanisms of alternans. Subcellular Ca alternans has been observed in experiments [27, 59, 85-87] and computer models [19, 59, 71, 88, 89], and tissue models with detailed cell models or multi-scale modeling approaches [59, 75, 77, 90-92] are needed to investigate how the subcellular Ca alternans dynamics affect the formation and synchronization of the APD-SDA and Ca-SDA patterns. We only use a global pacing protocol in which no action potential conduction exists. As we argued previously [50, 51], this pacing protocol not only has its own physiological realism but also provides a useful means for the understanding of the SDA dynamics when action potential conduction is present. We will carry out further investigations to include action potential conduction in the models to investigate how conduction and conduction restitution affect the SDA dynamics in the presence of Ca-driven alternans. We omitted the cell-to-Cell coupling of Ca in our models. It is known Ca can pass through the gap junction to the neighboring cells [62], and thus cell-to-cell Ca coupling exists. However, it is believed that this coupling is very weak, and therefore, it has been omitted in computational cardiac tissue models. Although the cell-to-cell Ca coupling may be weak, it may become nontrivial under certain conditions. Furthermore, if this coupling is not weak, it will affect the Ca-SDA patterns and their synchronization with APD-SDA patterns, which cannot be omitted. These need to be investigated in future studies. Finally, we only investigate the nodal line dynamics in the ionic tissue model using the Mahajan et al action potential model [61] in which the alternans is primarily driven by a Ca instability and the Ca-to-APD coupling is positive. We can change the Ca-to-APD coupling in the model to be negative by adding a Ca-activated small conductance potassium current as shown in our previous study [19]. However, under the negative coupling condition, we were still not able to generate quasiperiodicity in this model by simply changing the conductance of the L-type Ca current or any of the potassium currents, likely due to the lack of enough voltage-driven instabilities. Other ionic models may be used in future studies to investigate the coupled dynamics when both Ca-driven and voltage-driven instabilities are present to reveal the predictions from the AE model and the CML model.

V. Acknowledgements

This study was supported by National Institutes of Health grants R01 HL134709, R01 HL133294, and R01 HL157116 (Z.Q.); and Natural Science Foundation of China grant no. 82172067 (Z.S.) and Grant No. 71731002 (C.H.).

VI. Appendix. The CML and ionic models

1. The CML model

A CML model is an array of coupled iterated maps of APD and Ca. In a previous study [51, 80], we developed a CML model to describe the spatiotemporal dynamics of APD in 1D and 2D models. Here we use the same CML model to investigate the SDA dynamics in the presence of Ca-driven alternans.

a. The single-cell iterated map model

We use the iterated map model we developed previously [22] for APD and Ca dynamics in the presence of Ca and APD coupling. The equations are:

$$a_{n+1} = F(d_n, l_n, B_n) = f(d_n)(1 + \gamma c_{n+1}^p) \quad \text{(A1)}$$

$$l_{n+1} = l_n - q(d_n)g(l_n) + u(T)h(c_{n+1}^p) \quad \text{(A2)}$$

$$B_{n+1} = B_n - \kappa[c_n - c(T)] \quad \text{(A3)}$$

where a_{n+1} is the APD of the (n+1)th beat, and d_n is the DI of the nth beat, satisfying $d_n = T - a_n$. l_n is the SR Ca load at the end of the nth beat, and B_n is the total cytosolic Ca at

the end of the n[th] beat. c_n is the diastolic Ca at the end of the n[th] beat, which is described by

$$c_n = B_n - l_n \quad \text{(A4)}$$

c_{n+1}^p is the peak cytosolic Ca at the (n+1)[th] beat, which is described by

$$c_{n+1}^p = c_n + q(d_n)g(l_n) \quad \text{(A5)}$$

The functions are defined as follows:

$$f(d_n) = a_0 + a_1/(1 + e^{-\frac{d_n - d_0}{\tau_a}}) \quad \text{(A6)}$$

$$g(l_n) = l_n[1 - (1 - \alpha)/(1 + e^{\frac{l_n - l_0}{\beta}})] \quad \text{(A7)}$$

$$h(c_{n+1}^p) = \nu c_{n+1}^p[1 - 1/(1 + e^{\frac{c_{n+1}^p - c_0^p}{\delta}})] \quad \text{(A8)}$$

$$q(d_n) = 1 - \sigma_R e^{-d_n/\tau_q} \quad \text{(A9)}$$

$$u(T) = 1 - \rho e^{-T/\tau_u} \quad \text{(A10)}$$

$$c(T) = c_0(1 + \varepsilon e^{-\frac{T}{\tau_c}}) \quad \text{(A11)}$$

γ is the parameter describing Ca-to-APD coupling and σ_R is the one describing APD-to-Ca coupling. a_0, a_1, d_0, and τ_a in Eq.A6 are the parameters determining the APD and APD restitution properties. $a_0 = 50$ ms, $a_1 = 150$ ms, and $d_0 = 100$ ms are used. We change τ_a to alter the APD restitution properties. α and β are the parameters determining the fractional Ca release properties and we change β to change the fractional Ca release properties to promote Ca alternans. $\alpha = 0.036$, $\kappa = 0.2$, $\nu = 0.4$, $\delta = 20$, $\rho = 0.15$, $\varepsilon = 2$, $l_0 = 93.5$, $c_0^p = 50$, $c_0 = 28$, $\sigma_R = 0.4$, $\tau_q = 80$, $\tau_u = 200$, and $\tau_c = 300$. σ_R is altered for synchronization of APD-SDA and Ca-SDA. Note that the Greek letters α, β, ρ and ε are parameters specific to the iterated map model, not related to the same Greek letters in the AE model. The physiological meanings of the functions and parameters are detailed in the previous study [22].

b. The 1D cable CML model

Under global pacing, there is no conduction, and thus every cell in the cable has the same excitation period, which is just the pacing period *T*. Therefore, the DI and APD of a cell satisfy the following relationship:

$$d_n(i) = T - a_n(i) \quad \text{(A12)}$$

where *i* is the cell index in the cable and *n* is the beat number. Based on our previous formulation [51, 80], $a_n(i)$ is determined as follows:

$$a_n(i) = F_{n-1}(i) + \varepsilon \sum_{k=-M}^{M} w_k[F_{n-1}(i+k) - F_{n-1}(i)] \quad \text{(A13)}$$

where $F_n(i) = F[d_n(i), l_n(i), B_n(i)]$ is the function described in Eq.A1. ε is a parameter controlling the coupling strength of voltage between cells and *M* is the maximum coupling length (i.e., number of cells). w_k describes the distance-dependent weight of coupling strength, which is a Gaussian function, i.e., $w_k = \frac{e^{-k^2/2\sigma^2}}{\sqrt{2\pi}\sigma}$. We use $\varepsilon = 1$, $\sigma = 25$, and $M = 100$. No-flux boundary conditions are used. Details of the CML model and boundary conditions are presented in Wang et al [80].

2. The ionic model

1D cable and 2D tissue simulations are carried out using the rabbit ventricular action potential model by Mahajan et al [61]. The governing partial differential equation for voltage (*V*) in the 1D cable is:

$$\frac{\partial V}{\partial t} = -\frac{I_{ion} + I_{stim}}{C_m} + D\frac{\partial^2 V}{\partial x^2} \quad \text{(A16)}$$

where C_m=1 μF/cm^2, D=0.001 cm^2/ms, and I_{ion} is the total ionic current density from the rabbit ventricular action potential model by Mahajan et al [61]. I_{stim} is the stimulus current density, which is a 0.5 ms duration and -80 μA/cm^2 pulse applied periodically with a pacing period *T*. The governing partial differential equation for *V* in the isotropic 2D tissue model is:

$$\frac{\partial V}{\partial t} = -\frac{I_{ion} + I_{stim}}{C_m} + D\left(\frac{\partial^2 V}{\partial x^2} + \frac{\partial^2 V}{\partial y^2}\right) \quad \text{(A17)}$$

No-flux boundary conditions are used for both 1D and 2D tissue models.

*Email: zqu@mednet.ucla.edu.

References

[1] D. M. Bers, Cardiac excitation-contraction coupling, Nature **415**, 198 (2002).
[2] Z. Qu, G. Hu, A. Garfinkel, and J. N. Weiss, Nonlinear and stochastic dynamics in the heart, Phys Rep **543**, 61 (2014).
[3] L. Traube, Ein fall von pulsus bigeminus nebst bemerkungen tiber die lebershwellungen bei klappenfehlern und uber acute leberatrophic, Ber. Klin. Wschr. **9**, 185 (1872).
[4] H. E. Hering, Das Wesen des Herzalternans, Muenchener Med Wochenschr **4**, 1414 (1908).
[5] G. R. Mines, On dynamic equilibrium in the heart, J Physiol **46**, 349 (1913).
[6] J. B. Nolasco and R. W. Dahlen, A graphic method for the study of alternation in cardiac action potentials, J. Appl. Physiol. **25**, 191 (1968).
[7] M. R. Guevara, G. Ward, A. Shrier, and L. Glass, Electrical alternans and period doubling bifurcations, IEEE Comp. Cardiol. **562**, 167 (1984).
[8] L. Glass, Dynamics of cardiac arrhythmias, Physics Today **49**, 40 (1996).
[9] D. S. Rosenbaum, L. E. Jackson, J. M. Smith, H. Garan, J. N. Ruskin, and R. J. Cohen, Electrical alternans and vulnerability to ventricular arrhythmias, N Engl J Med **330**, 235 (1994).
[10] S. M. Narayan, T-wave alternans and the susceptibility to ventricular arrhythmias, J Am Coll Cardiol **47**, 269 (2006).
[11] X. Zhou, A. Bueno-Orovio, M. Orini, B. Hanson, M. Hayward, P. Taggart, P. D. Lambiase, K. Burrage, and B. Rodriguez, In vivo and in silico investigation into mechanisms of frequency dependence of repolarization alternans in human ventricular cardiomyocytes, Circ Res **118**, 266 (2016).
[12] P. K. Moore, K. E. Raffel, and I. R. Whitman, Macroscopic T-wave alternans: A red flag for code blue, JAMA Intern Med **177**, 1520 (2017).
[13] A. Vinet, D. R. Chialvo, D. C. Michaels, and J. Jalife, Nonlinear dynamics of rate-dependent activation in models of single cardiac cells, Circ. Res. **67**, 1510 (1990).

[14] Z. Qu, M. Nivala, and J. N. Weiss, Calcium alternans in cardiac myocytes: Order from disorder, J Mol Cell Cardiol **58**, 100 (2013).
[15] R. Rovetti, X. Cui, A. Garfinkel, J. N. Weiss, and Z. Qu, Spark-induced sparks as a mechanism of intracellular calcium alternans in cardiac myocytes, Circ Res **106**, 1582 (2010).
[16] E. Alvarez-Lacalle, I. R. Cantalapiedra, A. Penaranda, J. Cinca, L. Hove-Madsen, and B. Echebarria, Dependency of calcium alternans on ryanodine receptor refractoriness, PLoS One **8**, e55042 (2013).
[17] E. Alvarez-Lacalle, B. Echebarria, J. Spalding, and Y. Shiferaw, Calcium alternans is due to an order-disorder phase transition in cardiac cells, Phys Rev Lett **114**, 108101 (2015).
[18] M. A. Colman, C. Pinali, A. W. Trafford, H. Zhang, and A. Kitmitto, A computational model of spatio-temporal cardiac intracellular calcium handling with realistic structure and spatial flux distribution from sarcoplasmic reticulum and t-tubule reconstructions, PLoS Comput Biol **13**, e1005714 (2017).
[19] Z. Song and Z. Qu, Delayed global feedback in the genesis and stability of spatiotemporal excitation patterns in paced biological excitable media, PLoS Comput Biol **16**, e1007931 (2020).
[20] J. G. Restrepo, J. N. Weiss, and A. Karma, Calsequestrin-mediated mechanism for cellular calcium transient alternans, Biophys J **95**, 3767 (2008).
[21] Y. Shiferaw, D. Sato, and A. Karma, Coupled dynamics of voltage and calcium in paced cardiac cells, Phys Rev E **71**, 021903 (2005).
[22] Z. Qu, Y. Shiferaw, and J. N. Weiss, Nonlinear dynamics of cardiac excitation-contraction coupling: an iterated map study, Phys Rev E **75**, 011927 (2007).
[23] P. N. Jordan and D. J. Christini, Characterizing the contribution of voltage- and calcium-dependent coupling to action potential stability: implications for repolarization alternans, Am J Physiol Heart Circ Physiol **293**, H2109 (2007).
[24] I. Banville and R. A. Gray, Effect of action potential duration and conduction velocity restitution and their spatial dispersion on alternans and the stability of arrhythmias, J. Cardiovasc. Electrophysiol. **13**, 1141 (2002).
[25] M. E. Diaz, S. C. O'Neill, and D. A. Eisner, Sarcoplasmic reticulum calcium content fluctuation is the key to cardiac alternans, Circ Res **94**, 650 (2004).
[26] E. Picht, J. DeSantiago, L. A. Blatter, and D. M. Bers, Cardiac alternans do not rely on diastolic sarcoplasmic reticulum calcium content fluctuations, Circ Res **99**, 740 (2006).
[27] J. Kockskamper and L. A. Blatter, Subcellular Ca2+ alternans represents a novel mechanism for the generation of arrhythmogenic Ca2+ waves in cat atrial myocytes, J Physiol **545**, 65 (2002).
[28] Y. Li, M. E. Diaz, D. A. Eisner, and S. O'Neill, The effects of membrane potential, SR Ca2+ content and RyR responsiveness on systolic Ca2+ alternans in rat ventricular myocytes, J Physiol **587**, 1283 (2009).
[29] L. H. Xie, D. Sato, A. Garfinkel, Z. Qu, and J. N. Weiss, Intracellular Ca alternans: coordinated regulation by sarcoplasmic reticulum release, uptake, and leak, Biophys J **95**, 3100 (2008).
[30] E. Martinez-Hernandez, G. Kanaporis, and L. A. Blatter, Mechanism of carvedilol induced action potential and calcium alternans, Channels **16**, 97 (2022).
[31] J. M. Pastore, S. D. Girouard, K. R. Laurita, F. G. Akar, and D. S. Rosenbaum, Mechanism linking T-wave alternans to the genesis of cardiac fibrillation, Circulation **99**, 1385 (1999).
[32] J. M. Cao, Z. Qu, Y. H. Kim, T. J. Wu, A. Garfinkel, J. N. Weiss, H. S. Karagueuzian, and P. S. Chen, Spatiotemporal heterogeneity in the induction of ventricular fibrillation by rapid pacing: importance of cardiac restitution properties, Circ Res **84**, 1318 (1999).
[33] Z. Qu, A. Garfinkel, P. S. Chen, and J. N. Weiss, Mechanisms of discordant alternans and induction of reentry in simulated cardiac tissue, Circulation **102**, 1664 (2000).
[34] W. T. Clusin, Calcium and cardiac arrhythmias: DADs, EADs, and alternans, Crit Rev Clin Lab Sci **40**, 337 (2003).
[35] Z. Qu, Y. Xie, A. Garfinkel, and J. N. Weiss, T-wave alternans and arrhythmogenesis in cardiac diseases, Front Physiol **1**, 154 (2010).
[36] L. M. Muñoz, A. R. M. Gelzer, F. H. Fenton, W. Qian, W. Lin, R. F. Gilmour, and N. F. Otani, Discordant alternans as a mechanism for initiation of ventricular fibrillation in vitro, J Am Heart Assoc **7**, e007898 (2018).
[37] B. R. Choi, W. Jang, and G. Salama, Spatially discordant voltage alternans cause wavebreaks in ventricular fibrillation, Heart Rhythm **4**, 1057 (2007).
[38] W. Lu, T. Y. Kim, X. Huang, M. B. Liu, G. Koren, B. R. Choi, and Z. Qu, Mechanisms linking T-wave alternans to spontaneous initiation of ventricular arrhythmias in rabbit models of long QT syndrome, J Physiol **596**, 1341 (2018).
[39] M. A. Watanabe, F. H. Fenton, S. J. Evans, H. M. Hastings, and A. Karma, Mechanisms for discordant alternans, J Cardiovasc Electrophysiol **12**, 196 (2001).
[40] B. Echebarria and A. Karma, Instability and spatiotemporal dynamics of alternans in paced cardiac tissue, Phys Rev Lett **88**, 208101 (2002).
[41] J. J. Fox, M. L. Riccio, F. Hua, E. Bodenschatz, and R. F. Gilmour, Spatiotemporal transition to conduction block in canine ventricle, Circ Res **90**, 289 (2002).
[42] E. de Lange and J. P. Kucera, Alternans resonance and propagation block during supernormal conduction in cardiac tissue with decreased [K(+)](o), Biophys J **98**, 1129 (2010).
[43] B. Echebarria, G. Roder, H. Engel, J. Davidsen, and M. Bar, Supernormal conduction in cardiac tissue promotes concordant alternans and action potential bunching, Phys Rev E Stat Nonlin Soft Matter Phys **83**, 040902 (2011).
[44] H. Hayashi, Y. Shiferaw, D. Sato, M. Nihei, S. F. Lin, P. S. Chen, A. Garfinkel, J. N. Weiss, and Z. Qu, Dynamic origin of spatially discordant alternans in cardiac tissue, Biophys J **92**, 448 (2007).
[45] C. de Diego, R. K. Pai, A. S. Dave, A. Lynch, M. Thu, F. Chen, L. H. Xie, J. N. Weiss, and M. Valderrabano, Spatially discordant alternans in cardiomyocyte monolayers, Am J Physiol Heart Circ Physiol **294**, H1417 (2008).
[46] S. Mironov, J. Jalife, and E. G. Tolkacheva, Role of conduction velocity restitution and short-term memory in the development of action potential duration alternans in isolated rabbit hearts, Circulation **118**, 17 (2008).
[47] A. Gizzi, E. M. Cherry, R. F. Gilmour, Jr., S. Luther, S. Filippi, and F. H. Fenton, Effects of pacing site and stimulation

history on alternans dynamics and the development of complex spatiotemporal patterns in cardiac tissue, Front Physiol **4**, 71 (2013).
[48] O. Ziv, E. Morales, Y. K. Song, X. Peng, K. E. Odening, A. E. Buxton, A. Karma, G. Koren, and B. R. Choi, Origin of complex behaviour of spatially discordant alternans in a transgenic rabbit model of type 2 long QT syndrome, J Physiol **587**, 4661 (2009).
[49] E. Lau, K. Kossidas, T. Y. Kim, et al., Spatially Discordant Alternans and Arrhythmias in Tachypacing-Induced Cardiac Myopathy in Transgenic LQT1 Rabbits: The Importance of IKs and Ca2+ Cycling, PLoS One **10**, e0122754 (2015).
[50] C. Huang, Z. Song, J. Landaw, and Z. Qu, Spatially discordant repolarization alternans in the absence of conduction velocity restitution, Biophys J **118**, 2574 (2020).
[51] C. Huang, Z. Song, Z. Di, and Z. Qu, Stability of spatially discordant repolarization alternans in cardiac tissue, Chaos: An Interdisciplinary Journal of Nonlinear Science **30**, 123141 (2020).
[52] E. J. Pruvot, R. P. Katra, D. S. Rosenbaum, and K. R. Laurita, Role of calcium cycling versus restitution in the mechanism of repolarization alternans, Circ Res **94**, 1083 (2004).
[53] Z. Qu, M. B. Liu, R. Olcese, H. Karagueuzian, A. Garfinkel, P.-S. Chen, and J. N. Weiss, R-on-T and the initiation of reentry revisited: Integrating old and new concepts, Heart Rhythm **19**, 1369 (2022).
[54] F. G. Akar and D. S. Rosenbaum, Transmural electrophysiological heterogeneities underlying arrhythmogenesis in heart failure, Circ Res **93**, 638 (2003).
[55] K. R. Laurita and D. S. Rosenbaum, Interdependence of modulated dispersion and tissue structure in the mechanism of unidirectional block, Circ Res **87**, 922 (2000).
[56] Z. Qu, A. Garfinkel, and J. N. Weiss, Vulnerable window for conduction block in a one-dimensional cable of cardiac cells, 1: Single extrasystoles, Biophys J **91**, 793 (2006).
[57] Z. Qu, A. Garfinkel, and J. N. Weiss, Vulnerable window for conduction block in a one-dimensional cable of cardiac cells, 2: Multiple extrasystoles, Biophys J **91**, 805 (2006).
[58] D. Sato, Y. Shiferaw, A. Garfinkel, J. N. Weiss, Z. Qu, and A. Karma, Spatially discordant alternans in cardiac tissue. Role of calcium cycling, Circ Res **99**, 520 (2006).
[59] S. A. Gaeta, G. Bub, G. W. Abbott, and D. J. Christini, Dynamical mechanism for subcellular alternans in cardiac myocytes, Circ Res **105**, 335 (2009).
[60] D. Sato, D. M. Bers, and Y. Shiferaw, Formation of spatially discordant alternans due to fluctuations and diffusion of calcium, PLoS One **8**, e85365 (2014).
[61] A. Mahajan, Y. Shiferaw, D. Sato, et al., A rabbit ventricular action potential model replicating cardiac dynamics at rapid heart rates, Biophys. J. **94**, 392 (2008).
[62] P. A. Boyden, W. Dun, and B. D. Stuyvers, What is a Ca2+ wave? Is it like an Electrical Wave?, Arrhythmia & Electrophysiology Review 2015;4(1):35–9 (2015).
[63] S. K. Chua, P. C. Chang, M. Maruyama, et al., Small-conductance calcium-activated potassium channel and recurrent ventricular fibrillation in failing rabbit ventricles, Circ Res **108**, 971 (2011).
[64] X.-D. Zhang, D. K. Lieu, and N. Chiamvimonvat, Small-conductance Ca2+-activated K+ channels and cardiac arrhythmias, Heart Rhythm **12**, 1845 (2015).
[65] T. R. Shannon, K. S. Ginsburg, and D. M. Bers, Potentiation of fractional sarcoplasmic reticulum calcium release by total and free intra-sarcoplasmic reticulum calcium concentration, Biophys. J. **78**, 334 (2000).
[66] M. Nivala and Z. Qu, Calcium alternans in a couplon network model of ventricular myocytes: Role of sarcoplasmic reticulum load, Am J Physiol Heart Circ Physiol **303**, H341 (2012).
[67] H. R. Ramay, O. Z. Liu, and E. A. Sobie, Recovery of cardiac calcium release is controlled by sarcoplasmic reticulum refilling and ryanodine receptor sensitivity, Cardiovasc Res **91**, 598 (2011).
[68] E. A. Sobie, L. S. Song, and W. J. Lederer, Restitution of Ca(2+) release and vulnerability to arrhythmias, J Cardiovasc Electrophysiol **17 Suppl 1**, S64 (2006).
[69] A. Cely-Ortiz, J. I. Felice, L. A. Díaz-Zegarra, et al., Determinants of Ca2+ release restitution: Insights from genetically altered animals and mathematical modeling, J Gen Physiol **152** (2020).
[70] B. Echebarria and A. Karma, Amplitude equation approach to spatiotemporal dynamics of cardiac alternans, Phys Rev E Stat Nonlin Soft Matter Phys **76**, 051911 (2007).
[71] Y. Shiferaw and A. Karma, Turing instability mediated by voltage and calcium diffusion in paced cardiac cells, Proc Natl Acad Sci U S A **103**, 5670 (2006).
[72] J. Heijman, A. Zaza, D. M. Johnson, Y. Rudy, R. L. Peeters, P. G. Volders, and R. L. Westra, Determinants of beat-to-beat variability of repolarization duration in the canine ventricular myocyte: a computational analysis, PLoS Comput Biol **9**, e1003202 (2013).
[73] A. Skupin, H. Kettenmann, U. Winkler, M. Wartenberg, H. Sauer, S. C. Tovey, C. W. Taylor, and M. Falcke, How does intracellular Ca2+ oscillate: by chance or by the clock?, Biophys J **94**, 2404 (2008).
[74] M. Nivala, C. Ko, A. Garfinkel, J. N. Weiss, and Z. Qu, Self-organization of pacemaking sites for calcium waves and oscillations in cardiac myocytes, Biophys J **100**, 557a (2011).
[75] F. O. Campos, Y. Shiferaw, A. J. Prassl, P. M. Boyle, E. J. Vigmond, and G. Plank, Stochastic spontaneous calcium release events trigger premature ventricular complexes by overcoming electrotonic load, Cardiovasc Res **107**, 175 (2015).
[76] Z. Song, Z. Qu, and A. Karma, Stochastic initiation and termination of calcium-mediated triggered activity in cardiac myocytes, Proc Natl Acad Sci USA **114**, E270 (2017).
[77] M. A. Colman, Arrhythmia mechanisms and spontaneous calcium release: Bi-directional coupling between re-entrant and focal excitation, PLOS Comput Biol **15**, e1007260 (2019).
[78] M. Nivala, C. Y. Ko, M. Nivala, J. N. Weiss, and Z. Qu, Criticality in intracellular calcium signaling in cardiac myocytes, Biophys J **102**, 2433 (2012).
[79] H. Risken, *The Fokker-Planck Equation* (Springer, Berlin, 1989).
[80] S. Wang, Y. Xie, and Z. Qu, Coupled iterated map models of action potential dynamics in a one-dimensional cable of coupled cardiac cells, New J Phys **10**, 055001 (2007).

[81] A. R. Cram, H. M. Rao, and E. G. Tolkacheva, Toward prediction of the local onset of alternans in the heart, Biophys J **100**, 868 (2011).
[82] R. Visweswaran, S. D. McIntyre, K. Ramkrishnan, X. Zhao, and E. G. Tolkacheva, Spatiotemporal evolution and prediction of [Ca2+]i and APD alternans in isolated rabbit hearts, J Cardiovasc Electrophysiol **24**, 1287 (2013).
[83] Z. Qu, M. B. Liu, and M. Nivala, A unified theory of calcium alternans in ventricular myocytes, Scientific Reports **6**, 35625 (2016).
[84] J. Landaw and Z. Qu, Memory-induced nonlinear dynamics of excitation in cardiac diseases, Phys Rev E **97**, 042414 (2018).
[85] M. E. Diaz, D. A. Eisner, and S. C. O'Neill, Depressed ryanodine receptor activity increases variability and duration of the systolic Ca2+ transient in rat ventricular myocytes, Circ Res **91**, 585 (2002).
[86] L. H. Xie and J. N. Weiss, Arrhythmogenic consequences of intracellular calcium waves, Am J Physiol Heart Circ Physiol **297**, H997 (2009).
[87] G. L. Aistrup, Y. Shiferaw, S. Kapur, A. H. Kadish, and J. A. Wasserstrom, Mechanisms underlying the formation and dynamics of subcellular calcium alternans in the intact rat heart, Circ Res **104**, 639 (2009).
[88] Z. Song, M. B. Liu, and Z. Qu, Transverse tubular network structures in the genesis of intracellular calcium alternans and triggered activity in cardiac cells, J Mol Cell Cardiol **114**, 288 (2018).
[89] L. Romero, E. Alvarez-Lacalle, and Y. Shiferaw, Stochastic coupled map model of subcellular calcium cycling in cardiac cells, Chaos: An Interdisciplinary Journal of Nonlinear Science **29**, 023125 (2019).
[90] Z. Qu, A. Garfinkel, J. N. Weiss, and M. Nivala, Multi-scale modeling in biology: How to bridge the gaps between scales?, Prog Biophys Mol Biol **107**, 21 (2011).
[91] Y. Shiferaw, G. L. Aistrup, and J. A. Wasserstrom, Synchronization of triggered waves in atrial tissue, Biophys J **115**, 1130 (2018).
[92] M. A. Colman, E. Alvarez-Lacalle, B. Echebarria, D. Sato, H. Sutanto, and J. Heijman, Multi-scale computational modeling of spatial calcium handling from nanodomain to whole-heart: Overview and perspectives, Front Physiol **13** (2022).